Quantitative analysis of segmented satellite network architectures: A maritime surveillance case study

Juan A Fraire, Santiago Henn, Gregory Stock, Robin Ohs, Holger Hermanns, Felix Walter, Lynn van Broock, Gabriel Ruffini, Federico Machado, Pablo Serratti, et al.

Quantitative Analysis of Segmented Satellite Network Architectures: A Maritime Surveillance Case Study

Juan A. Fraire[a,b], Santiago Henn[a], Gregory Stock[c], Robin Ohs[c], Holger Hermanns[c], Felix Walter[d], Lynn Van Broock[e], Gabriel Ruffini[e], Federico Machado[f], Pablo Serratti[e], Jose Relloso[e]

[a]*CONICET – Universidad Nacional de Córdoba, Córdoba, Argentina*
[b]*Inria, INSA Lyon, CITI, UR3720, 69621 Villeurbanne, France*
[c]*Saarland University, Saarland Informatics Campus, 66123 Saarbrücken, Germany*
[d]*D3TN GmbH, 01159 Dresden, Germany*
[e]*INVAP S.E., Bariloche, Argentina*
[f]*CONAE, Córdoba, Argentina*

Abstract

This paper presents an in-depth trade-off analysis of a Swarm Satellite Constellation (SSC) Mission for Earth observation that leverages Segmented Architecture (SA), a concept designed by the Argentinian Space Agency (CONAE) within the New Space philosophy. This architecture consists of a scenario featuring a networked constellation of small, cooperative satellites to enhance mission flexibility, reliability, coverage, and cost-effectiveness. Despite its promising prospects, SA features challenges in its mission design and definition phases due to the complex interplay between distributed space systems, technological innovation, and geographical landscapes. Our study analyzes an innovative quantitative analysis framework integrated with Ansys' Systems Toolkit (STK). The resulting software tool models critical components, including ground and space segments, orbital dynamics, coverage, onboard processing, and communication links. We focus on a hypothetical SARE mission to detect illicit maritime activity near Argentina's Exclusive Economic Zone (EEZ). This case study constitutes an archetypal mission elucidating the architecture's benefits and complexities, addressing swarm coverage, contact dynamics, and data handling strategies. Results contribute to discussions on the practical trade-off in current and future Segmented Satellite Architectures with multiple mission objectives.

Keywords

Segmented architecture, Satellite constellations, Flight formation

1 Introduction

In February 2024, INVAP S.E., a lead satellite manufacturer from Argentina, hosted a MISSION workshop in San Carlos de Bariloche, Argentina. The Models in Space Systems: Integration, Operation, and Networking (MISSION) project,[1] funded by the EU's H2020 RISE program, aims to revolutionize space mission planning, design, and operations with cutting-edge software and networking models. MISSION comprises a consortium of Argentinian and European entities and provides a robust framework for tackling mission designs and analyses. It positions itself as a pivotal resource in advancing complex space mission architectures. The 2024 MISSION workshop gathered PhD students, professors, and engineers to analyze possible tools for tackling some of the challenges faced by a constellation of small satellites.

The workshop's core focus was on the so-called "Segmented Architecture", or SA. SA is an Earth observation mission framework led by the Argentinian Space Agency (CONAE) [1]. The SA is based on a Swarm Satellite Constellation (SSC) network of inexpensive, low-complexity, free-flying small satellites (between 100 and 250 kg), referred to as *segments*, that leverage state-of-the-art networking techniques to work cooperatively to achieve a common objective. This spatial distribution offers several benefits, such as improved flexibility, reliability, wider aperture measurements, extended coverage, and utilizing small-scale launchers like the ones developed by CONAE itself [2]. Inter-satellite links allow segments to share memory, processing functions, and downlink capabilities in orbit. The mission's Earth observation nature allows opportunistic data forwarding between the satellites, which contrasts with real-time immediate forwarding in typical communication constellations. Indeed, the main goal of the SA is to build autonomous and delay-tolerant wireless networks in space that operate with little to no real-time ground station intervention. The SA approach signifies a shift towards more flexible, cost-effective, and responsive space missions. Furthermore, the SA program represents CONAE's strategic advancement into the "New Space" context [3], building on the legacy of its missions based on large-scale satellites like SAOCOM 1A and 1B [4], and SAC-D Aquarius [5], among others.

While the Segmented Architecture concept embodies the dynamism and adaptability of CONAE's vision for multi-mission capabilities, it has also presented considerable challenges. The architecture's inherent flexibility has acted as its Achilles' heel. Despite concerted efforts, the materialization of specific missions within the SA program remains in flux amidst a complex political milieu and the constraints of finite resources in the region. As noted in academic discussions over the years, this concept's ongoing discourse and evaluation [6] underlines the intricate balance between space networking aspirations and the pragmatic facets of mission planning and execution. While project engineers possess the intuitive expertise to grasp the performance implications of

[1] MISSION Project URL: https://mission-project.eu. The MISSION project is an EU-funded initiative whose main objective is to gather Academia and Industry collaboratively to analyze technologies that could solve critical aspects of spacecraft design for future space missions of the European and global space industry.

This document is an author-generated version of a publication in Computer Networks 255 (2024). DOI: 10.1016/j.comnet.2024.110874

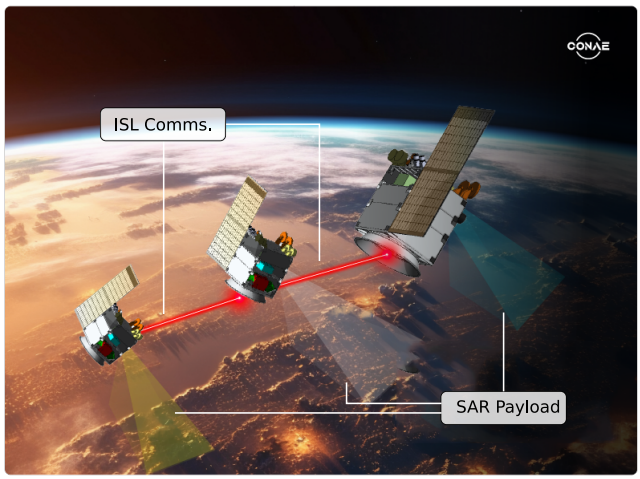

Figure 1: Conception of a cross-linked SA mission, based on synthetic aperture radio and comprising 100-to-250 kg-class spacecraft comprising a hypothetical SARE mission (adapted from: [1]).

various SA configurations qualitatively, there has been a noticeable gap in quantitatively assessing these configurations.

This paper aims to conduct a comprehensive trade-off analysis of the variables characterizing a mission architecture by leveraging MISSION expertise and the complexity of SA. Our modeling efforts provide a general quantitative evaluation framework for three Low-Earth Orbit (LEO) satellites flying standard X-band Synthetic Aperture Radar (SAR) payloads to detect targets that would be visible despite weather and sun incidence. Such could be the case of covert vessels illegally operating near Argentina's EEZ coastline, a problem that this country has been facing for decades [7]. Satellite-based SAR is widely regarded as the superior sensor for ship detection, given its capacity to produce resolutions commensurate with ship sizes, consistent wide-area imaging, and its independence from daily light cycles or cloud cover, ensuring uninterrupted monitoring in the variable marine climate [8, 9]. Research predominantly focuses on the direct detection of ship targets in SAR imagery, facilitated by the typically high radar reflectivity of ships [10]. While SAR is adept at locating bright, point-like targets indicating ships, it is also susceptible to speckle noise, which can obscure image details, necessitating advanced processing for clear interpretation [11, 12]. The integration of the SAR payload into the SA paradigm gives origin to a Swarm Satellite Constellation known as SARE, illustrated in Figure 1. This is the core case study we analyze throughout this paper.

Based on this SAR-based case study, we introduce a detailed software-based model that interfaces seamlessly with Ansys' Systems Toolkit (STK) [13], a renowned space mission simulation platform. Our model combines ground and space segment representations, incorporating realistic orbital mechanics and comprehensive coverage analytics. It incorporates sophisticated onboard processing simulations and communication models for Ground-to-Space Links (GSL) and Inter-Satellite Links (ISL). All model elements are framed so that analyzing other mission configurations is possible with minimal effort. The resulting software-based model enables us to provide the first quantitative performance assessment of the Segmented Architecture's advantages and complexities, offering insights into its first potential implementation.

This paper is organized as follows. Initially, Section 2 lays the foundational knowledge required for the Segmented Architecture. Subsequently, Section 3 delineates the STK-integrated software model specifically developed for detecting elusive vessels. Next, Section 4 delves into the analysis of the simulation results, providing critical insights into the mission's viability and effectiveness. Section 5 discusses the relevance of the analysis outcomes. Finally, the paper conclusions are provided in Section 6.

2 Background

Distributed Satellite Systems (DSS) represent a specialized mission architecture wherein spacecraft collaborate and share resources to accomplish a unified mission objective [14]. This architecture is relevant to Earth observation missions, particularly in expansive regions such as Argentina's EEZ. In this section, we delve into the concept of DSS by defining and illustrating examples of constellations and formations. Additionally, we discuss the motivations for monitoring the vast portion of the Atlantic Ocean within Argentina's EEZ. This background gives readers a comprehensive context of our research's underlying principles and objectives.

2.1 Constellations and Formations

Missions based on multiple satellites can be primarily categorized into two distinct operational paradigms: *constellations* and *formations* [15]. These approaches are united by their shared strategy of leveraging a group of spatially dispersed space vehicles for collective mission objectives [16, 17]. While constellations are distinguished by their extensive geographic reach, formations emphasize closer inter-satellite collaboration and coordination. Specifically:

- *Constellations*: They comprise a vast, spatially spread array of satellites strategically deployed to provide comprehensive global coverage. This is exemplified by networks such as the Starlink or Iridium systems, where the expansive distribution of satellites ensures a broad service range.
- *Formations*: Also known as clusters or swarms, they entail a more cohesive grouping of satellites. These satellites operate near each other, fulfilling roles such as part of a flying interferometer or facilitating material or data exchange, thereby concentrating their capabilities in a more confined area of space [18].

2.1.1 Constellations. Key common features and characteristics of constellations within the DSS context include:

- *Autonomy*: The operational autonomy of individual satellites, which may have ISL capability, allows for integrated communication and coordination within the fleet. These satellites are typically launched as a complete unit or in phased increments [19].
- *Distribution*: This is often realized through symmetrical arrangements, spacing N satellites $\frac{360}{N}$ degrees apart in anomaly and distributing them across P orbital planes, each

separated by $\frac{360}{P}$ degrees in Right Ascension of the Ascending Node (RAAN). The distances involved vary depending on the orbit, ranging from several hundred to thousands of kilometers in LEO and escalating to tens of thousands in higher orbits depending on the application [20].
- *Resilience*: The decentralized architecture in constellations, where functionalities are distributed among multiple orbiting satellites, inherently enhances system resilience. This distributed model fosters a form of natural redundancy, ensuring continued operation even in the event of individual satellite failures. Consequently, the system's overall performance degrades gracefully rather than failing abruptly [21].

Below, we discuss three characteristic examples of Satellite Communications, Earth Observation, and Navigation constellations.

- *Starlink (Satellite Communications).* Among the several constellations already operational, SpaceX's Starlink stands out as a monumental endeavor, representing the largest deployment of satellite communications (SatComs). The primary objective of this mega-constellation is to provide global broadband internet access. Leveraging an extensive network of LEO satellites, Starlink endeavors to deliver high-speed, low-latency internet connectivity, particularly to areas historically underserved by traditional infrastructure [22]. Other SatComs examples include OneWeb and O3B systems [23].
- *Iceye (Earth Observation).* Iceye, in contrast, directs its focus toward Earth observation capabilities. Employing SAR technology, Iceye's constellation enables imaging of the Earth's surface regardless of cloud cover or time of day. The resulting high-resolution data facilitates various applications, including environmental monitoring, maritime vessel tracking, and disaster response efforts [24].
- *Beidou (Navigation).* The China National Space Administration's (CNSA) Beidou constellation is a notable alternative to the US-operated Global Positioning System (GPS). Positioned in medium-Earth orbit (MEO), Beidou satellites furnish navigation and positioning services to civilian and military users across the globe, augmenting global positioning capabilities [25].

Choosing between *dense* and *sparse* configurations in satellite constellation design affects cost, coverage, latency, and complexity. On the one hand, dense constellations comprising 70 or more satellites in a compact orbital shell are crucial to minimizing coverage gaps and offering low latency and high revisit rates, ideal for real-time applications. However, they face challenges in satellite management, collision risk, and environmental impact [26, 27, 28]. On the other hand, sparse constellations use fewer satellites over a wider orbital area, reducing costs and collision risks but at the expense of increased latency and lower revisit frequency due to the increased coverage gaps. They provide broader coverage with fewer satellites, suitable for applications like navigation and asset tracking, but have limitations in data transfer and revisit times [29, 30, 31].

2.1.2 Formations. Although possibly to a lesser extent, the features of formations overlap with those mentioned for constellations while adding further aspects due to their physical proximity and task-sharing aspects [32]:

- *Formation Flying*: A critical aspect of formation systems involves maintaining precise spacecraft orientation. This necessitates a control law for tracking and maneuvering that is fundamentally interdependent, based at least on the state information of one other spacecraft in the group. A master satellite dictates the formation pattern, while slave satellites adjust accordingly [33]. In this paper, we use the terms *master/slave(s)*, but *leader/follower(s)* are also used in the literature.
- *Task Distribution*: Formations distribute functional capabilities across multiple spacecraft. This modular approach allows sharing resources such as memory, processing power, and sensor data through advanced wireless networking. This division of tasks among various spacecraft enables more versatile and efficient mission operations.
- *Rendezvous and Docking*: A potential feature of spacecraft formations is the necessity for rendezvous operations, where spacecraft adjust their trajectories to approach each other closely. In specific scenarios, this can extend to docking procedures, where spacecraft physically connect for purposes such as resource transfer, joint operations, or assembly of larger structures in space.

Next, we list a series of formation examples that have proven key technology enablers for formation flying:

- *TanDEM-X (SAR Mission)*: The TanDEM-X mission, a notable SAR endeavor, launched the German TDX satellite into orbit to form the first spaceborne bistatic interferometer alongside TerraSAR-X (TSX). This formation achieved advanced SAR data processing using the Integrated TanDEM-X Processor (ITP) to produce Raw Digital Elevation Models (DEM) [34].
- *CubeSat Demonstrations*: A series of nano-satellite missions were used as technological demonstrators for formation operations. (a) *AeroCube-4*: Conducted by the Aerospace Corporation, this mission involved three 1.2 kg 1 U CubeSats (1 U standing for one unit of 10 cm × 10 cm × 10 cm) demonstrating precise attitude control and innovative formation flight capabilities. The satellites could adjust drag profiles and adapt wing configurations [35]. (b) *Canadian Advanced Nanospace Experiments 4 and 5 (CanX-4&5)*: Led by the University of Toronto and the Canadian Space Agency, the CanX-4&5 mission demonstrated submeter tracking accuracy in formation flying [36]. (c) *AeroCube-OCSD*: Aimed at demonstrating optical communication and spacecraft tracking, this Aerospace Corporation mission utilized two 1.5 U CubeSats with advanced sensors and propulsion systems [37].
- *Proba-3 (Precision Formation Flying)*: The European Space Agency's Proba-3 mission focuses on high-precision satellite formation flying. It consists of two small satellites—the Coronagraph and the Occulter—designed to maintain formation with millimeter and arcsecond accuracy [38].

Formation flying in satellite operations manifests in three primary types: trailing, fractionated spacecraft, and clusters, each contributing uniquely to mission design and efficiency.

- *Trailing Formations*: In trailing formations, also known as *string of pearls*, satellites follow the same orbit at fixed intervals, facilitating communication and sharing similar orbital perturbations, enhancing operational stability.
- *Fractionated Spacecraft*: Fractionated spacecraft, exemplified by the F6 system (Future Fast, Flexible, Fractionated, Free-Flying Spacecraft united by Information exchange), splits a traditional monolithic spacecraft into separate functional units. With flexible launch strategies and modular designs, this design offers improved reliability through functional distribution and stronger survivability [39, 40].
- *Cluster*: Clusters consist of spacecraft groups not uniformly distributed in space, with the designation of being *tight* or *loose* based on their relative proximity. Clusters are gaining interest in applications such as asteroid prospection, requiring significant autonomy [41, 42].

Generally, any multi-spacecraft mission not classified as a formation is considered a constellation. Additionally, virtual or *Ad-Hoc* missions may emerge, where independently designed missions like Aqua, Aura & PARASOL, and later CloudSat, CALIPSO, GCOM-W1 & OCO-2, collaborate as though they are a single mission [20, 41].

2.2 Inter-Satellite Links (ISLs)

ISLs form critical networks for efficient in-orbit data routing, enhancing operation autonomy and reducing reliance on ground stations in satellite constellations and formations. ISL implementation considers mechanical (gimbal or body-pointing) or electrical beam steering for dynamic pointing geometries. Combined with other electrical factors such as antenna gain and power, these are relevant in defining the link budget and, thus, the effective data transmission rate. Additionally, the emergence of Free Space Optical (FSO) communication offers higher data rates and a license-free spectrum for ISLs [43, 44, 45].

Pointing Aspects. ISLs must be accurately pointed. Both RF and FSO laser communications systems in space demand precise Pointing, Acquisition, and Tracking (PAT) methods, with technologies like fast steering mirrors or gimbals for laser systems and varied solutions for RF antennas, each presenting unique challenges in space environments [18, 46, 47, 48]. As depicted in Figure 2, two satellites in the same orbit (along-track) exhibit consistent relative positions, simplifying communication. Satellites in adjacent orbits or varying orbital planes require precise alignment to maintain connection, which may involve complex tracking systems in different phases and inclinations or ascending/descending configurations.

Link Budget Aspects. For effective ISLs, a careful balance of antenna gain and transmission power is essential to ensure robust communication over the distances between satellites. This link budget must account for satellite altitude, bandwidth, and communication protocol. Popescu's analysis [49] highlights a fundamental trade-off in satellite communication: modifying data rates and transmission power to achieve optimal signal integrity. RF communication, being simpler and more traditional, often presents a more

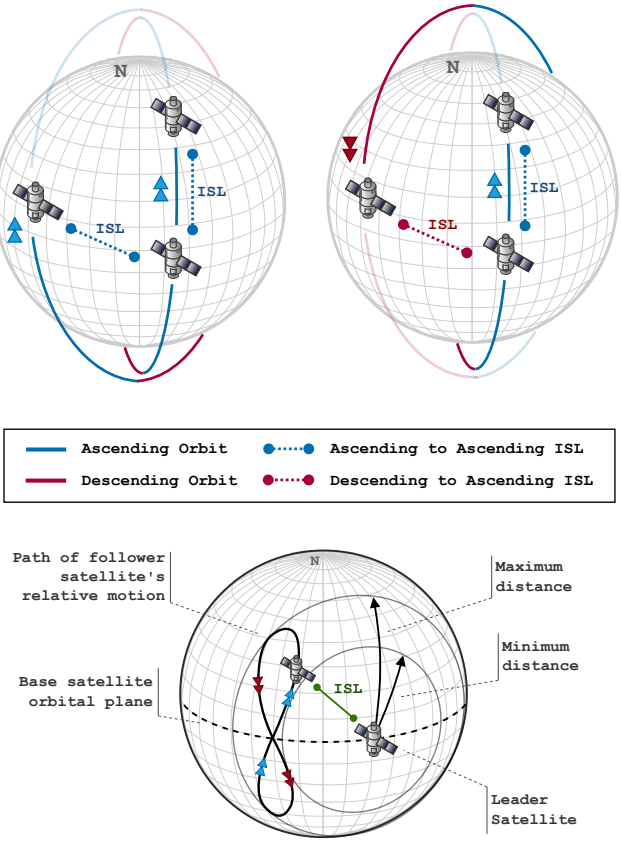

Figure 2: ISL dynamics. ISL between ascending satellites (top left). ISL between satellites in different planes (top right). ISL between two co-altitude satellites in circular orbits with relative phase and inclination differences (a.k.a., analemma pattern, bottom).

straightforward approach than FSO. While FSO communication offers higher data rates and a license-free spectrum, it must contend with atmospheric variables such as absorption, scattering, and turbulence, particularly in near-Earth environments [43, 44, 45]. These atmospheric effects can lead to signal attenuation and increased bit error rates. RF communication, in contrast, is less susceptible to atmospheric interference, making it a more straightforward and reliable option for many space applications.

2.3 Illegal Fishing in Argentina's EEZ

Illegal, unreported, and unregulated (IUU) fishing is a critical global concern, threatening marine ecosystems and economies with losses of up to 25 billion USD annually. IUU fishing is particularly problematic in Argentina's exclusive economic zones (EEZs), as well as in West African nations and the Northwest Pacific. Despite satellite transponder tracking capabilities, as illustrated in Figure 3, many vessels circumvent detection by disabling their Automatic Identification Systems (AIS), a tactic that directly undermines monitoring and regulatory efforts [50, 7]. Indeed, vessel movement analyses

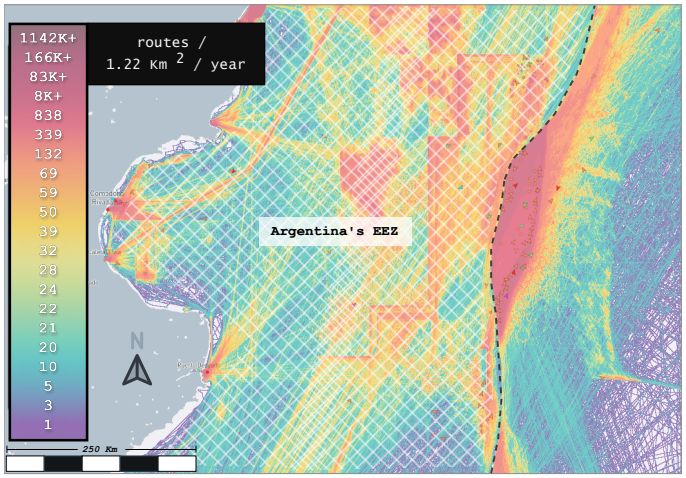

(a) Spatial analysis of vessel traffic highlighting areas where fishing vessels are densely concentrated along the EEZ.

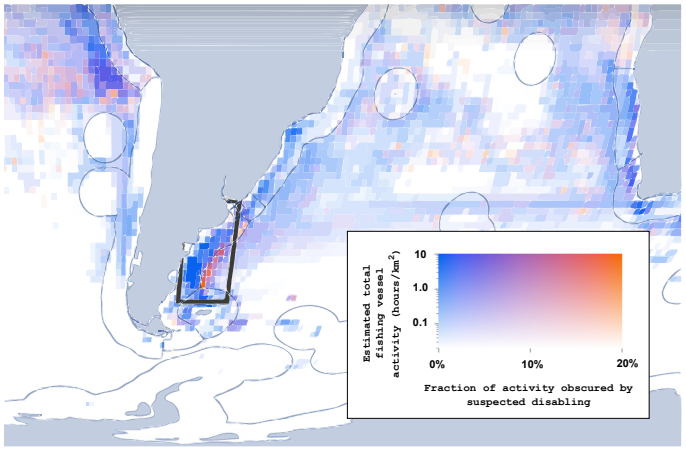

(b) Proportion of fishing operations likely obscured by deliberate AIS deactivation, signifying evasion attempts [50].

Figure 3: AIS Maritime data from [51].

indicate a clustering of fishing activity near EEZ boundaries, often crossing into restricted zones. While AIS is designed for collision avoidance, its adoption has also been crucial for fleet monitoring. However, intentional AIS deactivation poses significant challenges, with up to 20 % of vessels suspected of such practices in EEZ proximities, as depicted in Figure 3b, compromising surveillance and enforcement measures [51].

3 Model

The study in this paper focuses on a Segmented Architecture case study employing a trio of LEO satellites designed to detect elusive vessels off the coast of Argentina. We refer to this SA instantiation based on SAR imaging payloads as the SARE mission. Our approach entails developing an intricate modeling suite constructed from specialized, simpler models encompassing area analysis, orbital mechanics, communication links, and operational protocols. These individual components are seamlessly integrated using STK's Python API. This cohesive fusion results in a comprehensive, sophisticated, and flexible simulation of the entire SARE fleet mission. Indeed, enhanced by STK's granularity and flexibility, our model allows for a detailed and adaptable exploration of the mission's multifaceted dynamics, offering tailored analytical depth to meet the program's ambitious objectives.

3.1 Area of Interest Model

Leveraging STK, our coverage analysis rigorously determines the observability of assets over targeted maritime areas. The framework based on STK integrates grid points representing the Argentine coastline's EEZ and beyond, a region underscored by Milko Schvartzman's work[2] as critically affected by illegal fishing activities. The boundaries listed in Table 1 and illustrated in Figure 4 were manually extracted from Schvartzman's investigations.

[2]Schvartzman's Website: https://milkoschvartzman.wordpress.com/

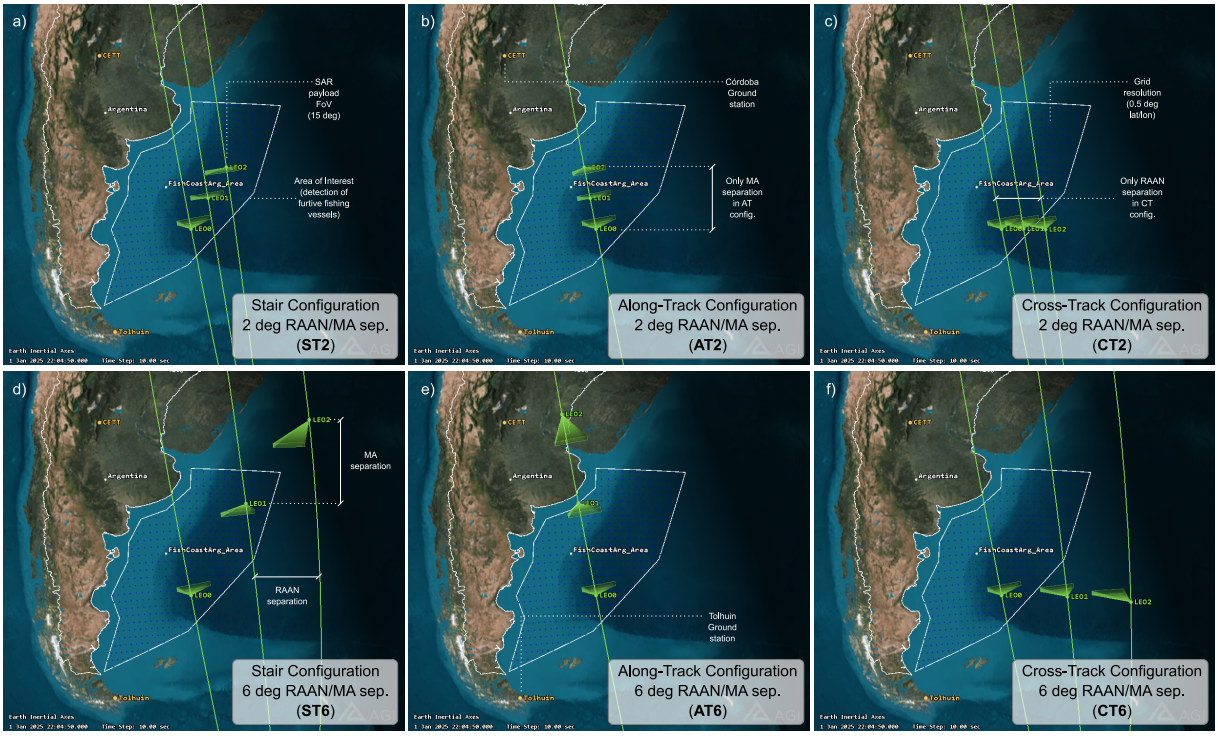

Figure 4: Overall Mission Model. Stair (ST), along-track (AT), and cross-track (CT) configurations for 2 and 6 degree RAAN/MA separation for the space segment. Ground stations and areas of interest are illustrated in all subfigures with relevant visual information.

Table 1: Area of interest (Argentina's fishing area) boundary coordinates, derived from Schvartzman's investigations.

Latitude	Longitude	Latitude	Longitude
−52.1°	−67.8°	−39.4°	−58.2°
−47.8°	−64.5°	−37.7°	−55.7°
−45.9°	−65.1°	−36.1°	−55.6°
−43.3°	−62.7°	−36.1°	−46.7°
−41.8°	−62.4°	−43.3°	−48.9°
−40.0°	−60.9°	−49.2°	−56.3°

By meticulously delineating this area of interest with an `AreaTarget` object in STK and setting a granular grid resolution of 0.5 degrees in latitude and longitude, the `CoverageDefinition` STK object (associated with the `FishCoastArg` area) calculates the potential satellite coverage. Our model is thereby calibrated to enhance the monitoring and safeguarding of these waters, ultimately aiding in the sustainable stewardship of marine life and mitigating illicit practices. Note that the area model is flexible and can be adapted to other areas with minor effort.

3.2 Ground Segment Model

The ground segment model includes two Argentine stations: the Córdoba Ground Station in the Teófilo Tabanera Space Center (CETT) and the Tierra del Fuego Ground Station near Tolhuin, in the country's southernmost region [52]. Both stations, illustrated in Figure 5, are instrumental in the country's space endeavors. Table 2 provides their exact location in our model. Both ground stations are configured with a 5-degree minimum elevation profile. The developed model is flexible to accommodate other parameters.

3.2.1 Córdoba Ground Station. The Córdoba Ground Station, located centrally within the country, is well-placed for satellite data acquisition over Argentina and its neighboring countries, including Chile, Bolivia, Paraguay, and Uruguay, as well as significant areas of Peru and Brazil. Its array of antennas, which includes sizes of 3.6 m, 7.3 m, and 13 m for Tracking, Telemetry, and Commands (TT&C) in the S band and downlink in X and S bands, enables it to perform various functions such as reception, processing, publication, and storage of satellite information.

3.2.2 Tolhuin Ground Station. The Tierra del Fuego Ground Station, being the southernmost on the continent, extends Argentina's reach for TT&C and data download capabilities, especially for polar orbits. It has a 13.5 m antenna operating in S, X, and Ka bands.

3.3 Space Segment Model

3.3.1 Orbital Configuration. The space segment model incorporates swarm configurations consisting of three LEO satellites with uniform Keplerian orbital parameters to represent a coordinated flight formation condition.

Figure 5: Córdoba Ground Station in the Teófilo Tabanera Space Center (CETT) (left) and Tierra del Fuego Ground Station near the town of Tolhuin (right). Source [52].

Table 2: Coordinates, altitudes, and minimum elevation profile of Córdoba and Tierra del Fuego Ground Stations.

Ground Station	Latitude	Longitude	Altitude	Min. Elev.
CETT	−31.524 986°	−64.462 739°	0.730 km	5.0°
Tolhuin	−54.510 448°	−67.115 565°	0.140 km	5.0°

Sun-Synchronous Orbits. The space segment design incorporates circular Sun-Synchronous Orbits (SSO) to maintain a consistent solar illumination profile, streamlining the energy management system. This approach aligns with CONAE's established protocols for LEO missions. The satellites are positioned at an altitude of 550 km, resulting in a semi-major axis of 6921 km. The satellites are deployed at an inclination of 97.0356 degrees to ensure sun synchronicity at this orbital height [53].

Flight Formations. We manipulate the Right Ascension of the Ascending Node (RAAN) and the True Anomaly (TA) angles to develop diversified swarm topologies. True Anomaly and Mean Anomaly (MA) can be used interchangeably in circular orbits (0 eccentricity). The Argument of Periapsis is kept at 0 degrees. This strategy delineates three principal configuration groups, each encompassing four distinct variations:

- *Along-Track (AT)*: This configuration is characterized by Mean Anomaly separations of 2, 4, 6, and 8 degrees. The resulting formation resembles a train, where satellites follow one another along the orbit track, with the distance between satellites expanding as the Mean Anomaly separation increases. Depending on the Mean Anomaly angular separation, we refer to this configuration as AT2, AT4, AT6, and AT8.
- *Cross-Track (CT)*: By adjusting the RAAN angle in increments of 2, 4, 6, and 8 degrees, we generate swarms that extend parallel to the equatorial plane, resulting in satellites arranged side by side (as seen from a velocity vector perspective). This configuration is consequently called CT2, CT4, CT6, and CT8.

Table 3: Orbital Parameters for AT, CT, and ST Configurations. Other common parameters include eccentricity (0) and Argument of Perigee (0°).

Config. (sep.)	Alt.	Inc.	M. Anom.	RAAN
AT2, AT4, AT6, AT8	550 km	97.0356°	2°, 4°, 6°, 8°	0°
CT2, CT4, CT6, CT8	550 km	97.0356°	0°	2°, 4°, 6°, 8°
ST2, ST4, ST6, ST8	550 km	97.0356°	2°, 4°, 6°, 8°	2°, 4°, 6°, 8°

- *Stair (ST)*: A hybrid of AT and CT configurations is achieved by varying both RAAN and Mean Anomaly angles. This creates a "stair" shaped topology, positioning satellites in a staggered formation that incorporates both forward and lateral separations [6]. As a result, the stair formation is encoded as ST2, ST4, ST6, and ST8.

These formations were selected to account for existing mission capabilities and the potential for improved spatial and temporal coverage in the SARE mission. Thus, they provide a broader and more flexible framework for performance analysis than conventional approaches. For example, the A-Train constellation and TanDEM-X/TerraSAR-X follow an AT approach, while communication constellations like Iridium and Globalstar exemplify Cross-Track configurations with multiple RAAN planes. However, our proposed ST configuration goes beyond current practice, offering a novel combination of RAAN and Mean Anomaly separations, which is not found in existing constellations like Sentinel-1 and Cosmo-SkyMed, which remain in the same orbital plane.

The main orbital parameters are summarized in Table 3. Figure 4 illustrates each group separating 2 and 6 degrees in RAAN and Mean Anomaly (RAAN/MA). Obtained from the STK user interface, this figure provides a real-scale representation of the distances involved in the overall scenario, including ISL ranges, the area of interest, and the two ground stations involved.

Propagator. We utilize the SGP-4 propagator in STK to compute the orbital trajectories, which offers a more accurate representation

of orbital dynamics for long-term analysis. SGP-4 accounts for essential perturbations such as atmospheric drag, Earth's oblateness, third-body effects (from the Moon and Sun), and solar radiation pressure. This propagator is well-suited for our year-long analysis, where formation-keeping maneuvers are assumed to maintain stability in the operational SSO orbits. The framework remains flexible, allowing us to adjust parameters and repeat the quantitative analysis.

3.3.2 SAR Payload. SAR systems consist of a side-looking radar that acquires surface information in two-dimensional directions (i.e., azimuth and range) by successively transmitting electromagnetic pulses in the microwave spectrum and measuring the scattering echoes. SAR systems have a day-and-night imaging capability, and their wavelengths of microwave radiation (in the order of centimeters) are generally unaffected by weather conditions, allowing them to acquire images where optical images would be affected, for example, in regions with cloud coverage or low sunlight exposure [12, 11, 54].

As an active microwave sensing instrument, SARs rely solely on the energy they emit for operation. As such, SAR missions can specify parameters such as frequency, look angle, polarization, and the FOV of the SAR satellite, which is instrumental in determining the satellite potential applications, e.g., ship detection [54, 12].

SAR instruments' L, C, and X bands are the most widely employed frequencies. SARs generally transmit and receive linearly polarized signals, either horizontally (H) or vertically (V) polarized. Early SAR instruments operated in a single polarization mode, either VV (vertical transmission and vertical reception) or HH (horizontal transmission and horizontal reception). Recent and modern SARs provide dual- and quad-polarized images, which allows the generation of multiple images of the same scene [54].

The most critical SAR parameters for ship detection are resolution, incidence angle, polarization, and frequency [10]. Ships, being complex metallic structures, interact with the SAR signal via three physical scattering models:

- *Single-bounce returns*, due to direct backscattering from surfaces perpendicular to the radar beam.
- *Double-bounce returns*, due to the dihedral formed by the vertical ship's conducting plates and the sea surface.
- *Multiple-bounce returns*, caused by the ship's structure (e.g., deck and cables).

For these reasons, a vessel appears as a cluster of bright pixels in a SAR image with few identifiable features [55, 56, 57]. However, numerous studies in the literature are focusing on X-band SAR images (e.g., COSMO-SkyMed, Terra-X) for ship monitoring [56, 58, 59, 60], including research conducted in Argentine waters [61, 62]. HH polarization gives the best results among the classical polarizations when the incidence angle is larger than 45 degrees. At the same time, the cross-polarized (HV and VH) data are best when the incidence angle is below 45 degrees [10]. As a first approximation, taking a single channel from an X-band satellite is feasible, and ship detection can be conducted with typical approaches designed for single-polarized SAR images.

SAR Coverage. The SAR payload onboard our satellite operates at an X-band frequency and is renowned for its balance between resolution and penetration capabilities. Specifically, this payload is designed to instantaneously capture a swath of 11 km. However, if mechanically feasible, the SAR can adjust its orientation between 2 and 15 degrees during each satellite pass. This adjustment expands the field of regard—the total observable area by the sensor when it alters its pointing direction—across the ground track, potentially covering up to approximately 100 km, thanks to the radar's 1.2-degree 3 dB beamwidth.

Table 4: Specifications of the SAR Payload.

Parameter	Value
Frequency Band	X band
Instantaneous Swath Width	11 km
Field of Regard	up to 100 km
Beamwidth	1.2° at 3 dB
Data Acquisition Rate	120 Mega samples per second
Sample Digitization	12 bits per sample
Raw Data Generation Rate	1440 Mbps (180 MB/s)

While this flexibility in orientation increases potential coverage, it is important to emphasize that the actual field of view is significantly narrower, typically limited to 11 km. However, managing the pointing of the field of view is a matter of SAR operations, which is beyond the scope of this paper. To simplify the analysis, the remainder of this paper considers access to the entire field of regard (2 to 15 degrees). The results, therefore, reflect a best-case scenario where the spacecraft fully utilizes the entire field of regard and can rapidly adjust its pointing angle. In practice, however, only a small portion of this field of regard is observable at any given time, and pointing adjustments will require time, depending on the spacecraft's design. Future work will optimize the data acquisition plan with SAR operations to provide a more conservative and realistic estimation of the mission's performance.

SAR Data Generation Rate. The SAR system is configured for a data acquisition rate of 120 Mega Samples per second. Each sample is digitized at 12 bits, which results in a substantial raw data generation rate of 1440 Mbps or 180 MB/s, directly impacting the data storage and downlink requirements. Managing this high data rate is vital to the SAR payload operation, ensuring that the valuable information captured is efficiently processed, stored, and transmitted back to Earth for analysis.

The parameters of the SAR payload are summarized in Table 4. Based on these, we model the SAR payload as a rectangular nadir-pointing sensor in STK with 15- and 2-degree angles (see the green sensors in Figure 4).

3.4 Communications Model

This section addresses the crucial connectivity between the satellite fleet and ground stations.

3.4.1 Ground-to-Satellite Link (GSL). The Córdoba and Tolhuin ground stations are configured with a minimum elevation angle of 5 degrees to ensure a clear line of sight for communication links. The GSL utilizes the S-band frequency for telemetry and telecommand (TT&C) operations, but this paper focuses on the SAR payload

Table 5: Link Parameters for GSL and ISL.

Symbol	Description	GSL	ISL
f_c	Center Frequency	8.25 GHz	2.2 GHz
P_t	Transmitter Power	33 dBm	32 dBm
G_t	Transmitter Antenna Gain	13 dBi	8 dBi
G_r	Receiver Antenna Gain	58.7 dBi	8 dBi
B	Bandwidth	500 MHz	265 MHz
NF	Receiver Noise Figure	2 dB	2.5 dB
$R_{\max}$	Maximum data rate	225 Mbps	7.5 Mbps

data handling. Our model employs the X band for a high-volume payload data downlink facilitated by the high-gain 13 m antennas at both ground sites. We model the gain of the parabolic antenna with the following equation:

$$G_r = 10\log_{10}\left((D\lambda)^2\right) + 10\log_{10}(\eta). \tag{1}$$

A gain $G_r = 58.7$ dB is achievable for 8.25 GHz central frequency and a typical antenna efficiency ($\eta = 0.6$). We have crafted our X-band GSL downlink transmitter model around GomSpace's solutions tailored for nano- and micro-satellites. In particular, we utilize the capabilities of the *NanoCom Link X*, a Software-Defined Radio (SDR) platform paired with a reconfigurable X-band antenna module renowned for its versatility and high performance.[3] The NanoCom Link X can deliver raw transmission rates up to 225 Mbps, leveraging DVB-S2 modulation standards.

3.4.2 Inter-Satellite Link (ISL). We have opted for S-band communications for the ISL and defined critical parameters based on state-of-the-art commercial technology for nano- and small-satellites. As with GSLs, we consider the GomSpace NanoCom SR2000 SDR transponder, which integrates a Xilinx Zynq7000 FPGA with dual-core ARM processors. In this case, the SDR integrates with the ANT2000 S-band antenna. The resulting solution delivers cross-link data rates up to 7.5 Mbps, power efficiency, and reliable ISL data transfer based on CCSDS standards.[4] This ISL setup was successfully flight-tested in the GOMX-4 mission [63] and optimized with innovative automatic hands-off operation concepts [64, 65] by the authors. Due to potential cross-border regulatory aspects (out of the scope of this paper), we consider ISLs to be used when the fleet is over the Argentine territory.

The most relevant GSL and ISL parameters extracted from the reference GomSpace solutions are summarized in Table 5.

Size, Weight, and Power Considerations. While the NanoCom X and S communication solutions are optimized for compact nanosatellites, adhering to constraints like the 6U CubeSat standard, we justify their applicability within the SARE mission requirements and restrictions as follows. On the mechanical side, the SARE mission primarily focuses on integrating an advanced X-band SAR payload, potentially incorporating a deployable antenna mechanism, which can demand significant weight and volume budgets. On the power side, as indicated by literature in the field [63, 64], the collective energy demands for the NanoCom systems—encompassing one transponder for GSL and two for ISLs per spacecraft—align more closely with the power budgets of larger satellites rather than the typical CubeSat, reflecting the power profile considerations required for swarm platforms.

3.4.3 Link Budget Model. Shannon's theorem [66] estimates a communication link's maximum achievable capacity (information or data rate) under varying conditions without relying on specific details regarding the modulation and coding schemes.[5] This theorem provides an upper bound on the data rate achieved over a noisy channel with a specific bandwidth and Signal-to-Noise Ratio (SNR).

Signal-to-Noise Ratio (SNR). The SNR at the receiver is an essential component of Shannon's theorem estimation. The SNR is calculated using the received power (P_r) and noise power (P_n):

$$\text{SNR} = \frac{P_r}{P_n} = \frac{P_t + G_t + G_r - L_{fs}}{-174 + 10\log_{10}(B) + \text{NF}} \tag{2}$$

where the free-space path loss L_{fs} depends on the range d and the center frequency f:

$$L_{fs} = 20\log_{10}\left(\frac{4\pi d f_c}{c}\right) \tag{3}$$

Maximum Data Rate Estimation. Shannon's theorem states that the maximum data rate (R_{sha}) of a channel is determined by its bandwidth (B) and the SNR:

$$R_{\text{sha}} = B\log_2(1 + \text{SNR}). \tag{4}$$

This formula provides the theoretical upper limit of the data rate that can be transmitted over a communication channel with a given bandwidth and SNR, assuming an ideal (error-free) coding scheme. In our link model, we cap the GSL and ISL data rate based on the transceiver technological specifications defined in GomSpace's data sheets: $R = \min(R_{\text{sha}}, R_{\max})$. Figure 6 presents the resulting data rate for different ranges considering the parameters in Table 5. The maximum achievable data rate for the ISL is 7.5 Mbps for ranges up to ≈450 km, with Shannon's theorem defining the limits for extended distances. For example, 400 and 200 kbps are the theoretical bounds at the 2000 and 3000 km ISL range, respectively. These results consider that ISL antennas are respectively pointed, which might require body-pointing (or gimbal) mechanisms, especially for ST and CT configurations. In contrast, the GSL benefits from a significant link budget margin afforded by the 13 m diameter ground antennas with satellite-tracking capability, ensuring a robust 225 Mbps capability across operational ranges.

3.5 Operations Model

Our research delves into data handling strategies without restrictions (unconstrained) and within the limits of system capabilities (constrained). The constrained operations reflect scenarios akin to current operational conditions, where only one master satellite can

[3] GomSpace X-Band Solution (NanoCom Link X): https://gomspace.com/shop/subsystems/communication-systems/nanocom-link-x.aspx

[4] GomSpace S-Band Solution (NanoCom Link S): https://gomspace.com/shop/subsystems/communication-systems/nanocom-link-s.aspx

[5] While Shannon's theorem gives the theoretical maximum data rate, it's important to note that achieving this rate in practice is challenging. Real-world factors such as suboptimal coding, hardware imperfections, and environmental conditions often reduce the achievable data rate below this theoretical maximum. However, this model is particularly useful for understanding the upper limits of communication system performance and for comparing the efficiency of different system designs under the same operational conditions.

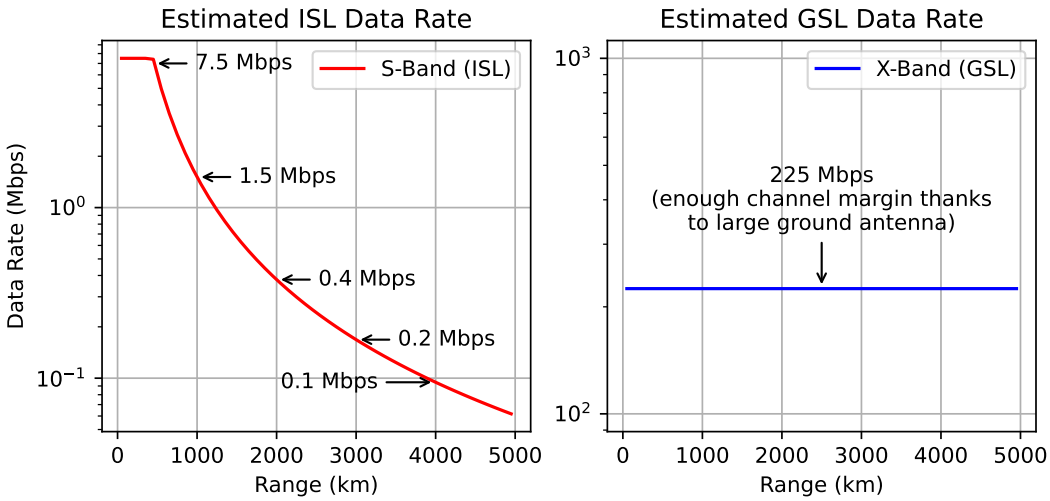

Figure 6: Data rate for GSL and ISL links obtained from our simplified link model based on the theoretical Shannon's theorem.

downlink data via an X-band receiver—mirroring a typical ground station setup. Here, we assess the impact of different data management approaches: direct transmission of raw data, application of data compression to reduce the data volume to 20 % or 10 %, and execution of on-board processing to distill data into concise reports.

In detail, we simulate two main scenarios: one where all satellites in the constellation (denoted as AD, for *all downlink*) can downlink data, and another where only a designated master satellite (indicated as MD, specifically the central satellite LEO1) performs this function. We assume data can be downlinked even when the SAR payload is operative and capturing data. In the MD configuration, the flanking satellites (LEO0 and LEO2) forward their gathered data to LEO1, which then forwards the SAR acquisition data to the ground station. In these cases, we assume automated store-carry-and-forward data handling, which can be covered by Delay-Tolerant Networking (DTN) technologies and protocols [67, 68]. We evaluate these approaches against various data conditions, including raw data downloads, data compressed to 20 % (Comp02) and 10 % (Comp01) of the original size, and a streamlined onboard processing scenario (Proc), which transmits a compact 200-byte summary after each 10-second SAR data collection. This analysis will ascertain the most efficient data handling method, considering satellite operations' bandwidth constraints and storage capacities.

3.6 Performance Metrics

3.6.1 Area Coverage. The cumulative coverage time is the first intuitive performance coverage metric. It measures the cumulative duration of covering any part of the area of interest. However, in the proposed configurations, each LEO satellite is equipped with identical payload capabilities, resulting in the same Field of Regard (FoR), and follows similar orbital trajectories characterized by circular orbits of equal altitude and inclination. Consequently, the cumulative coverage times across satellites are expected to be comparable, on average, in all formations. Therefore, we have chosen not to prioritize this metric as the central criterion for our analysis.

Revisit Time. Instead, we concentrate on Revisit Time as the key metric for comparing coverage across configurations. The Revisit Time metric measures the intervals when a specific area (defined by a series of grid points) is not covered by satellite observation, known as *coverage gaps*. The dynamic definition calculates the duration of the current gap at each grid point, with a gap duration of zero when a grid point is currently accessible. Therefore, the Revisit Time more accurately reflects the effectiveness of each swarm configuration in maintaining consistent surveillance and ensuring minimal coverage gaps, which is essential for timely and effective monitoring of the designated area. We consider these types of Revisit Time:

- The *average* Revisit Time for each grid point is calculated as the mean of all gap durations within the coverage period, represented by the equation: $\frac{\sum_{i=0}^{N} \text{GapDuration}_i}{N}$.
- The *maximum* Revisit Time at each grid point is determined by the longest coverage gap over the entire interval.
- The *minimum* Revisit Time at each grid point corresponds to the shortest gap in coverage encountered throughout the coverage interval.

These options provide a nuanced understanding of coverage gaps over the analysis interval, allowing for a detailed assessment of the satellite system's observational capabilities and limitations. This metric is particularly valuable for assessing the effectiveness of the Segmented Architecture in maintaining consistent surveillance, especially in critical applications like maritime monitoring.

However, we acknowledge that using more robust metrics, such as percentile-based revisit times (e.g., 5th and 95th percentiles) and the harmonic mean for revisit time aggregation, would provide a more consistent and accurate assessment by reducing the influence of outliers and accounting for varying observation frequencies.

Nevertheless, in this study, we have relied on these computations in our current analysis due to the limitations of the STK v12.5 Python interface, which supports only simpler metrics like average, maximum, and minimum. Future work will explore the possibility of manually exporting access times and calculating both percentile-based statistics and harmonic means to provide a more refined evaluation of coverage consistency and revisit statistics.

3.6.2 Contacts and Accesses. In our performance metrics evaluation, STK is pivotal in calculating the duration and ranges of contacts (visibility episodes between assets) and accesses (visibility episodes between an asset and an area).

Contact Duration. Contact duration measures how long a satellite communicates with a ground station or another satellite. Understanding the temporal aspects of data transfer capabilities and mission responsiveness is crucial. STK computes this by analyzing the line-of-sight visibility periods between entities, considering the satellite's orbital path, the ground station's location, minimum elevation constraints, and Earth obstructions. In STK, the computation of contact periods is akin to a binary search, where the software iteratively narrows down the search interval to pinpoint the precise start and end times of contact with configurable accuracy down to a millisecond tolerance.

Contact Range. Conversely, contact range represents the physical distance between satellites or between a satellite and a ground station during the access period. Once the contact period is established, STK samples within this window at configured time steps—in our model case, every 10 seconds—to accurately record the range values between the entities. This metric gives insights into the distance statistics during communication and access windows between the swarm, ground station, and areas of interest. These computed distances are vital for feeding the GSL and ISL communication model and deriving the effective data rate, leading to the data handling performance assessment we discuss below.

Swarm Contact. We define a *swarm contact* as the time interval where at least one of the satellites in the fleet can access any of the ground stations or the area of interest. This facilitates an integrated analysis of the joint fleet connectivity between satellites, ground stations, and areas of interest. This is particularly relevant in the current scenario as access to the fishing areas, visibility with the ground stations, and the ISLs co-occur due to the geographical proximity of these elements.

3.6.3 Data Handling. We rigorously evaluate data handling efficiency through key performance indicators: memory usage over time, the timeliness of data delivery, and the volume of data delivered daily per spacecraft. These metrics are scrutinized across two operational paradigms: All-Download (AD), where each satellite transmits data independently, and Master-Download (MD), with a designated master satellite handling all downlinks. Within these paradigms, our analysis spans the spectrum from raw, uncompressed data to various compression levels and an on-board processing option that succinctly compiles a 200-byte report for every SAR acquisition cycle lasting 10 seconds.

Table 6: Revisit Time values. Minimum, average, and maximum revisit times averaged among all the area of interest grid points.

Swarm Config.	Minimum (avg. hrs.)	Average (avg. hrs.)	Maximum (avg. hrs.)
ST2	0.01 h	25.44 h	326.34 h
ST4	6.04 h	25.32 h	211.34 h
ST6	5.93 h	25.17 h	121.61 h
ST8	6.20 h	25.10 h	96.84 h
AT2	0.01 h	25.46 h	434.31 h
AT4	0.02 h	25.42 h	427.16 h
AT6	0.02 h	25.43 h	420.04 h
AT8	0.03 h	25.43 h	412.68 h
CT2	5.22 h	36.81 h	333.61 h
CT4	5.91 h	25.36 h	225.43 h
CT6	5.96 h	25.20 h	131.25 h
CT8	6.01 h	25.18 h	85.26 h

4 Results

4.1 Simulation Environment

Our simulation environment leverages the robust modeling and analysis framework of STK. The defined scenario traces a year-long period beginning January 1, 2025, with a span of 365 days, ensuring a statistically significant evaluation of satellite passes over the designated ground stations and areas of interest. The computational capabilities of Python notebooks enhance the analysis. They enable intricate mission modeling and analysis and facilitate the transparency and reproducibility of our research.

4.2 Area Coverage

The analysis of Revisit Time as depicted in Figure 7 and quantified in Table 6 showcases the coverage capabilities of different satellite configurations (ST, AT, CT) with varying RAAN/MA separations (2, 4, 6, 8). The numerical data reveal the range and distribution of Revisit Times, highlighting how different configurations impact the frequency of satellite coverage at each grid point. The boxplot visually compares these configurations, depicting their coverage efficiency in the monitored area using the average, maximum, and minimum Revisit Time statistics.

4.2.1 Small Angular Separations. The analysis of lower RAAN/MA angular separations (e.g., 2 degrees) among the ST, AT, and CT configurations reveals a nuanced pattern of satellite coverage. For instance, the ST2 configuration's minimal Revisit Time of 0.01 hours indicates nearly continuous acquisition capabilities at specific grid points. This is expected, as close-by satellites will revisit the same point with a few seconds difference in a packed swarm formation. However, a maximum average Revisit Time of 326 hours for the ST2 configuration suggests considerable worst-case intervals between observations. Although configurations like ST2, AT2, and CT2 with 2-degree angular separations offer many potential access periods to the area of interest, they are tightly clustered, leading to extended

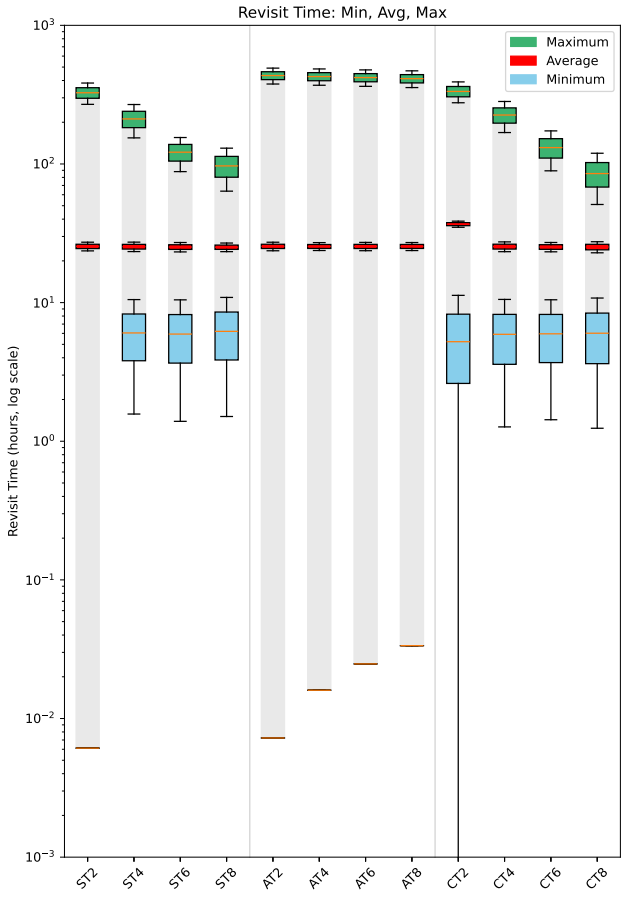

Figure 7: Revisit Time. Whisker plots for minimum, average, and maximum revisit times across all the area of interest grid points. A light gray area in the background presents the range of revisit time for all grid points for each flight segment configuration.

periods without coverage. CT2 presents overlapped coverage regions to the point that the minimum revisit gaps are zero, so the whisker plot escapes the logarithmic scale of the figure. The comparative analysis underscores that while average Revisit Times are similar across configurations, the distribution of maximum Revisit Times differs drastically, reflecting the unique coverage dynamics of each satellite constellation setup.

4.2.2 Large Angular Separations. Configurations with larger RAAN/MA separations (e.g., 8 degrees) result in a narrower range of Revisit Times, creating a more predictable and regular coverage pattern. Despite this, the average Revisit Time across different configurations remains relatively consistent, hovering around 25 hours. However, the extremes of Revisit Times exhibit greater sensitivity to changes in configuration, as evidenced by the AT configuration's maximum, which is on the order of 420 hours, no matter the angular separation. The CT8 configuration stands out with the shortest maximum Revisit Time of approximately 85 hours, showcasing the most uniform coverage. The ST8 configuration follows closely with a metric of 96 hours. These findings illustrate the intricate coverage balance between satellite configuration and coverage efficacy, presenting a complex decision-making scenario for the segmented architecture mission planners, even without assessing the technicalities of contacts and data transfer. Indeed, each configuration adjustment can lead to significant variations in surveillance performance.

4.2.3 Geographical Distribution. Figure 8 portrays the heatmaps of Maximum Revisit Time for the satellite configurations ST, AT, and CT, explicitly focusing on the more extreme 2- and 8-degree separation cases. This visual analysis has been chosen to highlight the worst-case scenario for revisit times across the area of interest. This is a critical factor in reasonable mission design aimed at minimizing the most extended intervals between satellite observations at any point. The variation in Maximum Revisit Time is visually encoded with distinct color scales optimized for each configuration, enhancing the contrast and allowing for a clearer understanding of geographic distribution patterns. The figure underscores that the chosen swarm formation/configuration substantially influences the spread of maximum revisit times within the monitored region. Specifically, the 2-degree separation case exhibits uniformity in the average maximum revisit time (as shown in Figure 7) and geographic distribution, which is evidenced in Figure 8. Conversely, the 8-degree separation cases reveal a pronounced disparity in revisit times across the grid points, especially when comparing the stair, along-track, and cross-track swarm configurations, indicating the significant impact of satellite formation on coverage patterns. The AT8 configuration resembles the ST2, AT2, and CT2 swarms. Naturally, these packed swarms provide similar maximum revisit time metrics to a single LEO satellite.

4.2.4 Swarm Configuration Selection. Based on this coverage analysis, we have strategically selected specific configurations for deeper examination. CT8 is chosen for its exemplary performance, yielding the shortest maximum Revisit Time of 85.26 hours. ST2 stands out among the 2-degree separation configurations, presenting the lowest maximum Revisit Time within its group at 326.34 hours. Its selection is underpinned by the expected superior ISL performance associated with reduced satellite-to-satellite distances, thus making ST2 the prime candidate for representing this category. ST8 demonstrates the second-shortest maximum Revisit Time at 96.84 hours and offers a valuable comparative analysis to ST2. Employing the same stair formation, ST8 allows us to discern the impact of broader angular separation on coverage quality and ISL complexity. We will specifically consider these formations in the following subsections.

4.3 Contacts and Accesses

4.3.1 Contact Duration. We analyze the duration of each GSL and area access contact individually and then, on a joint basis, consider the overall swarm contact.

Individual Contact Duration. A comprehensive simulation of the satellite configurations over a year yielded detailed contact duration profiles, as illustrated in the histograms of Figure 9. In the histograms, contact times for the Córdoba and Tolhuin ground stations, which require a minimum 5-degree elevation for operation,

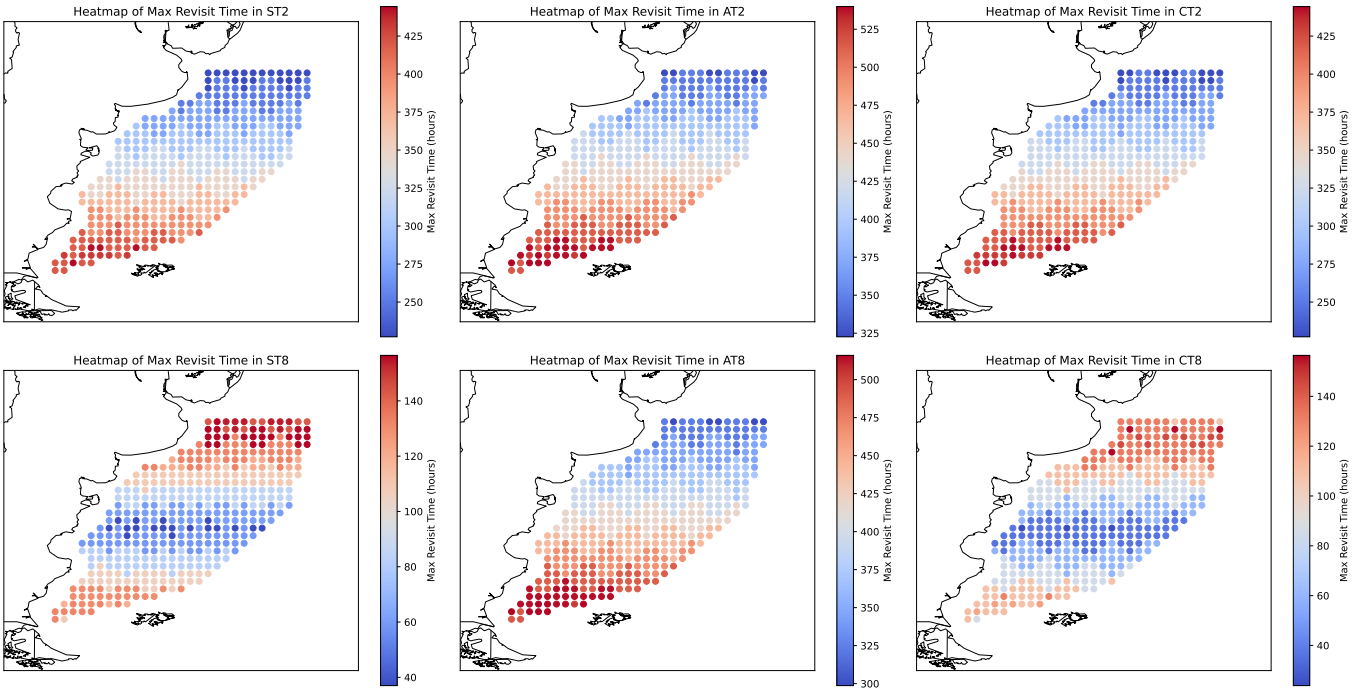

Figure 8: Maximum Revisit Times heatmaps for ST, AT, and CT in the 2 deg and 8 deg separation flavors. Each grid point in the area of interest is color-coded with the maximum Revisit Times recorded in the simulation period. Note color scales are different for each configuration to provide better contrast.

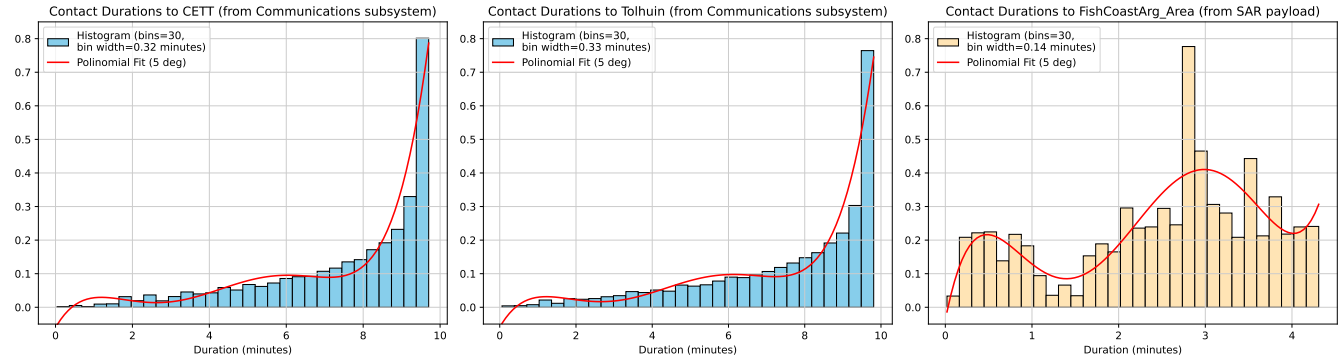

Figure 9: Individual contact duration distributions for all LEO satellites in all configurations to CETT and Tolhuin ground stations (5 deg minimum elevation each) and the target fishing area from the SAR payload (15 deg and 2 deg FoR). A polynomial fit of 5 degrees is offered as a visual guide for the histogram tendencies.

predominantly fall into a range starting from 4 minutes and peak near a modal duration of almost 10 minutes. The histogram reveals a pronounced peak in access to the targeted fishing area at around 3 minutes. This is primarily attributed to the limited swath width of the SAR payload, which spans 15 degrees of field of regard. This confinement dictates the brief yet regular access intervals, highlighting the interplay between payload capacity and observational opportunity.

Swarm Contact Duration. The number of swarm contacts (set of joint overlapping contacts between the fleet and ground stations, see Section 3.6.2) observed during the year for the selected configurations ST2, ST8, and CT8 is presented in Table 7. The findings underscore the enhanced access advantages of swarms with larger separations, as evidenced by the increased contact count and a more significant share of coverage over the area of interest. Notably, configurations with 8-degree separations yield more contacts and extend the duration of access to the designated fishing zones.

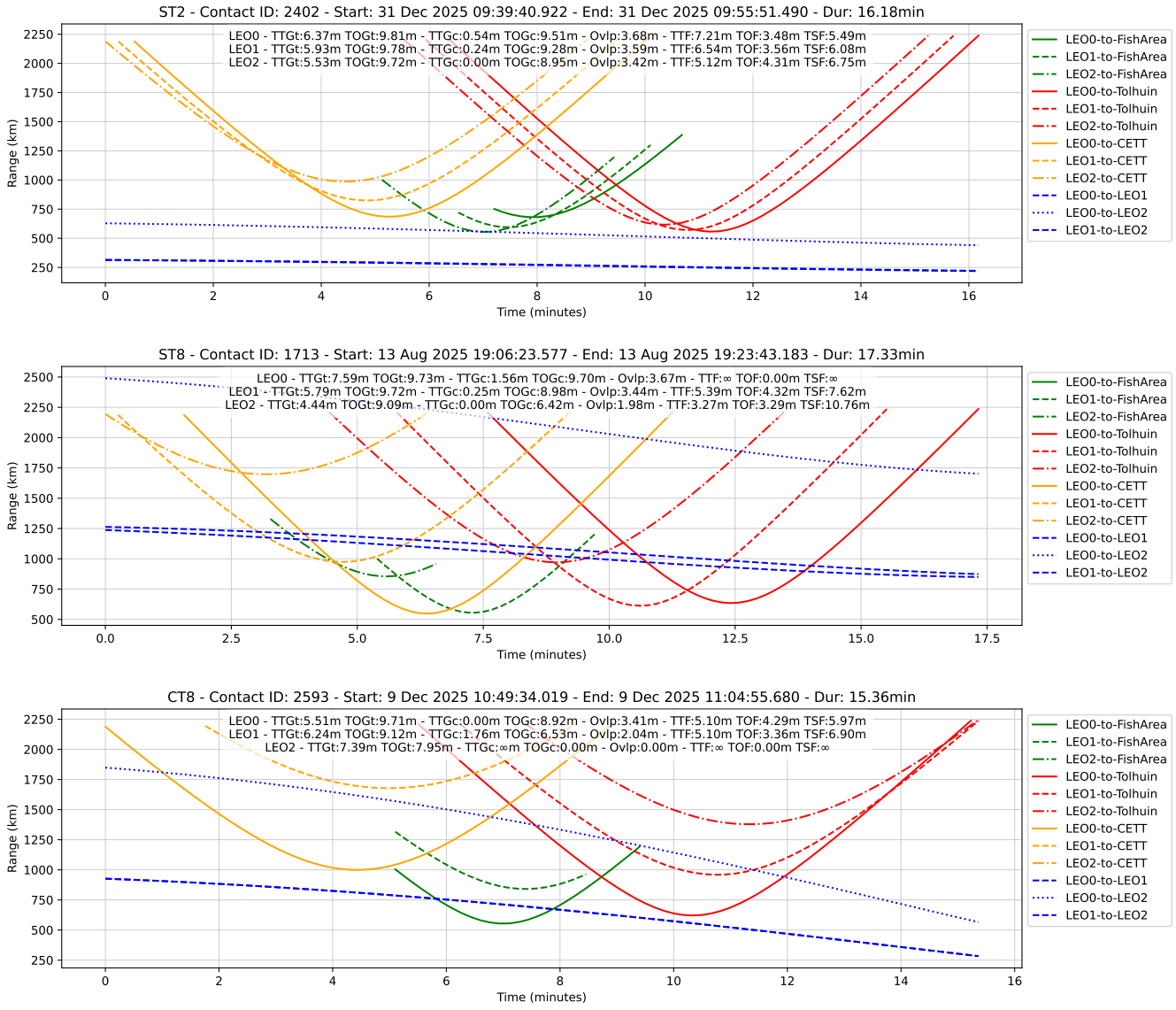

Figure 10: Example swarm contact range dynamics. These plots present the swarm contact range with the largest Time On Fish (TOF) recorded during the simulation year for the chosen ST2 (top), ST8 (center), and CT8 (bottom) configurations.

Table 7: Swarm Contact statistics. Contact count presented yearly and daily. All of these contacts include access to at least one ground station. A subset of those contacts include access to the area of interest.

Swarm Config.	Yearly Contacts	Daily Contacts	Yearly Area Access	Daily Area Access
ST2	2406	6.59	899 (37 %)	2.46
ST8	2786	7.63	1286 (47 %)	3.52
CT8	2757	7.55	1246 (45 %)	3.41

4.3.2 Contact Ranges. We focus on the shortlisted ST2, ST8, and CT8 configurations to address the contact ranges analysis.

Example Swarm Contacts. To gain intuition on swarm contacts, Figure 10 displays swarm contact range dynamics, highlighting the passes with the longest Time On Fish area (TOF) observed in our simulation. The time-related metrics Time To Fish (TTF) and Time Since Fish (TSF) are also provided to identify the context of the observed range value. Additionally, the metrics of Time To Ground (TTG) and Time On Ground (TOG) provide insights into the contact initiation and duration with the Córdoba and Tolhuin ground stations. See Table 8 for a summary of the meaning of these acronyms. These examples correspond to descending passes (from North to

Table 8: Time to/on/since Fish and Time to/on Ground.

Acronym	Description
TTF	Time To Fish: Duration from the beginning of the swarm's contact with the ground station until the satellites start monitoring the fishing area.
TOF	Time On Fish area: Duration of active satellite observation over the fishing area.
TSF	Time Since Fish: Time elapsed from when the satellites stop monitoring the fishing area until the end of the swarm's contact period.
TTG	Time To Ground: Time from the start of the swarm contact until a satellite gains visibility to a ground station.
TOG	Time On Ground: Duration of the satellite's communication link with the ground station once contact is established.

South), as Córdoba is visited first, then Tolhuin. Conversely, during ascending passes, this sequence is reversed. The overlap metric (Ovlp) measures the period when satellites are simultaneously in contact with both stations, which is crucial for optimizing network redundancy and making critical scheduling decisions, such as selecting the appropriate ground station for communication. The graphical representation also delineates the ISL distances throughout the swarm contact, showcasing the dynamic nature of satellite communications in various orbital configurations.

The quantitative outcomes from our simulations solidify the foundational understanding of swarm dynamics for the intended mission architecture. Regarding GSL, the ST2 configuration demonstrates more packed ground station contacts, attributable to the swarm's minimal RAAN/MA separation. Conversely, the ST8 and CT8 configurations exhibit more temporally and spatially dispersed access events. In all cases, GSL ranges are below the 2250 km threshold. For ISL, the proximity requirements are less stringent in the ST2 configuration, as evidenced by reported distances of approximately 300 km between adjacent satellites (LEO0-to-LEO1 and LEO1-to-LEO2) and up to 700 km across the swarm (LEO0-to-LEO2). With an 8-degree separation, neighboring ISL distances increase, reaching up to 1250 km for ST8 and 1000 km for CT8, respectively. The distinction is that ST8's stair-step formation necessitates managing two-dimensional separations (along-track and cross-track), while CT8's challenges are confined to along-track.

Beyond the three example contacts, and consistently across all swarm contacts observed during the year, there is an invariable presence of contact with at least one ground station concurrent with any LEO satellite's access to the fishing area. Also, we confirm that the duration of access to the fishing zone (TOF) is invariably shorter than that of the ground station link (TOG), a fact that not only corroborates the data in Figure 9 but also contextualizes it temporally.

Fish Time Distribution. Figure 11 elucidates the distribution and yearly accumulated values of Time To Fish (TTF), Time On Fish (TOF), and Time Since Fish (TSF) for the ST2, ST8, and CT8 configurations. While the distributions do not diverge markedly across the configurations, a steady correlation emerges among the TTF, TOF, and TSF values. On average, TTF hovers around 6 minutes, TOF at approximately 3 minutes, and TSF lingers between 7 and 8 minutes, underscoring a consistent pattern of satellite availability and observational potential across the configurations. We observe that ST8 excels at TSF, which makes it appealing to download data after passing over the area of interest.

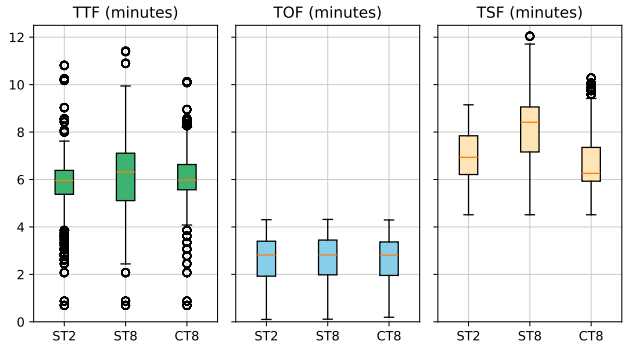

Metric	Config.	Avg.	Accum.
TTF	ST2	5.74 min	217.69 h
TTF	ST8	6.06 min	230.46 h
TTF	CT8	6.07 min	230.48 h
TOF	ST2	2.56 min	97.16 h
TOF	ST8	2.59 min	98.23 h
TOF	CT8	2.59 min	98.50 h
TSF	ST2	7.03 min	266.65 h
TSF	ST8	8.11 min	308.07 h
TSF	CT8	6.76 min	256.71 h

Figure 11: Time To Fish (TTF), Time On Fish (TOF), and Time Since Fish (TSF) distributions across all selected configurations. The table presents the numerical average values and the accumulated time throughout the simulated year.

ISL Range Distribution. Figure 12 illustrates the ISL distance distributions for 1-hop (between adjacent satellites) and 2-hop (across the swarm) during periods when the satellite swarm is in contact with ground stations. The 1-hop analysis encompasses direct neighbors (LEO0-LEO1 and LEO1-LEO2), while the 2-hop evaluation spans the furthest pairs (LEO0-LEO2). The ST configurations exhibit evident disparities in ISL performance, with 2-degree separations maintaining 1-hop distances under 320 km and 8-degree separations extending up to 1200 km. As discussed in Figure 6, these separation degree variations sharply contrast and directly affect ISL data rates. Notably, the CT8 configuration frequently positions 2-hop distances between LEO0 and LEO2 within a 600 km range, creating conditions that resemble the values of the more compact ST2 setup.

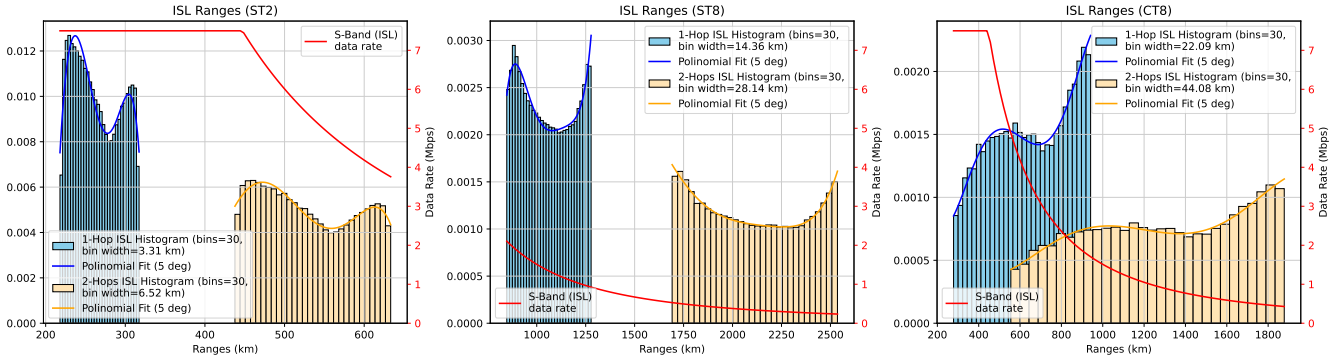

Figure 12: ISL range distributions for 1-hop (LEO0-LEO1 and LEO1-LEO2) and 2-hops (LEO0-LEO2) distances for the selected configurations (ST2, ST8, CT8) during the contact swarm contact with the ground stations.A polynomial fit of 5 degrees is offered as a visual guide for the histogram tendencies. The ISL data rate from Figure 6 is plotted for reference.

4.4 Data Handling

Our study investigates both unconstrained and constrained data handling scenarios. For constrained operations, we consider scenarios where a single master satellite serves as the exclusive downlink conduit, reflecting the real-world limitation of having just one X-band receiver at the ground stations. This framework examines the implications of handling raw data, utilizing various data compression levels, and implementing on-board processing policies.

4.4.1 Unconstrained Operations. Table 9 delineates the maximum data volume capabilities across different satellite formations, distinguishing between Area of Interest (AOI), Ground-Satellite-Link (GSL), and Inter-Satellite Link (ISL) access types. Notably, formations with larger RAAN/MA separations—such as ST8 for AOI and GSL—yield higher daily data volumes, with ST8 excelling in AOI data capture due to its 8-degree separation in RAAN/MA, as opposed to CT8's separation in RAAN alone. Conversely, the ST2 configuration, with a 2-degree separation in RAAN/MA, dominates in ISL data volumes, a trend also reflected in the close-range potential of the CT8 cross-track formation near the poles. The table also provides average data rates; ST2 consistently operates at the ISL's maximum rate of 7.5 Mbps, while CT8 occasionally reaches this cap. ST8's maximum ISL data rate caps at 2.1 Mbps.

Table 9 indicates that the GSL data volume can manage the total output from SAR for all configurations, assuming each satellite employs the X-band downlink concurrently. This presupposes the dual ground stations in Córdoba and Tolhuin are equipped with three X-band receiver chains to handle simultaneous operations, which is not the case, as discussed in Section 3. Furthermore, the table's data presuppose the simultaneous occurrence of SAR acquisitions, ISLs, and GSLs across the swarm—a generous assumption regarding the operational capacity of a small satellite platform.

4.4.2 Constrained Operations. We evaluate operational constraints by examining scenarios where either all satellites (AD) engage in downlinking data or solely the master satellite (MD)—designated as the central satellite, LEO1—undertakes this task. In the MD approach, the outer satellites (LEO0 and LEO2) relay their data to LEO1 via ISLs for subsequent ground transmission. We explore

Table 9: Data volume and data rate data handling statistics for selected configurations. ISL1 and ISL2 stand for 1- and 2-hop ISL distances. Min Max values are given only for ISLs as they might differ from the average value.

Config	Access	Data Volume (Daily)	Data Rate (Avg. (Min/Max))
ST2	AOI	27.98 GB	1440.0 Mbps
ST2	ISL1	1.45 GB	7.5 (7.5/7.5) Mbps
ST2	ISL2	1.09 GB	5.5 (3.8/7.5) Mbps
ST2	GSL	99.82 GB	225.0 Mbps
ST8	AOI	38.15 GB	1440.0 Mbps
ST8	ISL1	0.47 GB	1.4 (0.9/2.1) Mbps
ST8	ISL2	0.12 GB	0.4 (0.2/0.5) Mbps
ST8	GSL	123.17 GB	225.0 Mbps
CT8	AOI	37.43 GB	1440.0 Mbps
CT8	ISL1	1.22 GB	4.3 (1.7/7.5) Mbps
CT8	ISL2	0.37 GB	1.3 (0.4/4.9) Mbps
CT8	GSL	118.72 GB	225.0 Mbps

data handling efficiencies by considering raw data download (Raw), data compressed to 20 % (Comp02) and 10 % (Comp01) of its original volume, and an onboard processing (Proc) scenario where only a 200-byte classification report is transmitted following every 10-second SAR data acquisition.

Memory. Figure 13 depicts on-board memory usage during the initial 30 days for various data handling strategies. The AD-Raw configuration is uniquely capable of managing raw SAR downloads, despite memory surges reaching 20 GB, as all satellites in the formation can successfully transmit data to the ground. Conversely, the MD-Raw scenario, where only the master satellite downloads data, proves unfeasible. Memory usage for LEO0 and LEO2 quickly exceeds the 20 GB threshold without recovery, indicating that ISL capacity is a limiting factor in this model. Compression strategies (Comp01 and Comp02) vary in efficiency. The ST2 configuration performs well with a 10 % compression ratio but struggles at 20 %, while

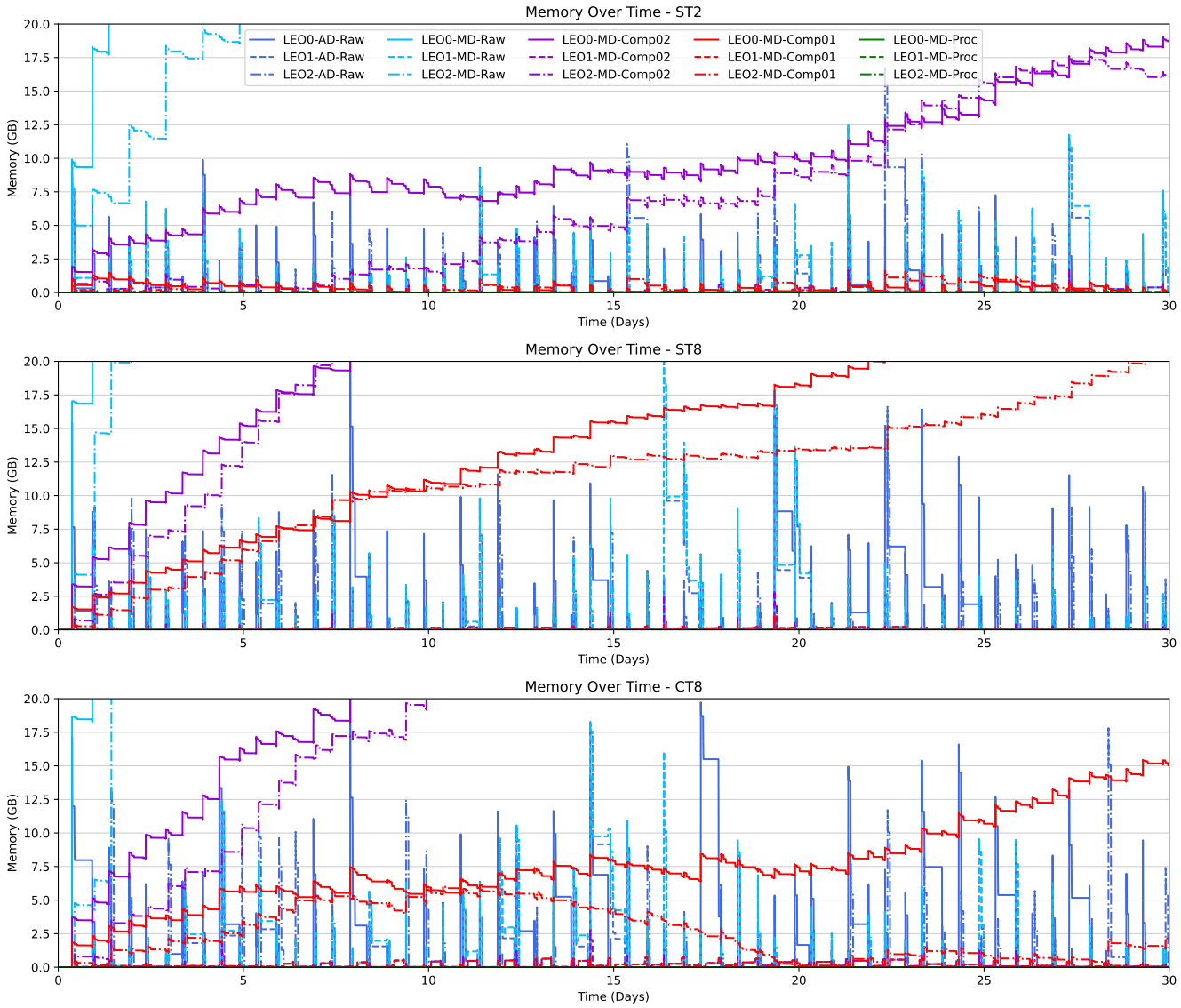

Figure 13: Memory evolution for the first month for the selected configurations (ST2, ST8, CT8). Raw data handling presents the highest spikes during acquisition, followed by Comp, which reduces them by 0.2 and 0.1. Proc only uses 200 bytes, leaving memory utilization near zero.

ST8 fails to offload at either compression rate due to inadequate ISL performance, as evidenced in Table 9. CT8 shows improved ISL throughput, successfully offloading data compressed to 10 %, though LEO0 cannot fully offload its SAR data. The MD-Proc method demonstrates an insignificantly small memory footprint in Figure 13, underlining its superiority as a strategy across all configurations examined.

Latency. Table 10 overviews the acquisition delivery delay and the daily delivery count for various swarm configurations and operational policies throughout the year. In the AD operation scenarios, the acquisition delivery latencies are minimal, which aligns with expectations since each satellite has direct downlink capabilities. Under the MD policy, where only the master satellite communicates with ground stations, delivery delays increase noticeably. ST2 exhibits minimal latency due to superior ISL performance in the packed swarm, while ST8 and CT8 experience average delays extending to about an hour, often requiring the next pass for data offload. Compression strategies marginally affect delivery delay but enhance the number of daily deliveries. Notably, onboard processing policies (MD-Proc) significantly outperform other methods, offering lower delivery delays and a drastic increase in the daily acquisition count, benefiting from the smaller data sizes after processing.

Table 10: Aquisition delivery delay and daily count for all evaluated configurations over the year.

Swarm	Operations	Delivery Delay		Daily
Config	Policy	Avg.	Max.	Count
ST2	AD-Raw	0.05 min	0.42 min	12
ST8	AD-Raw	0.05 min	0.42 min	14
CT8	AD-Raw	0.05 min	0.40 min	14
ST2	MD-Raw	11.67 min	680.12 min	6
ST8	MD-Raw	46.41 min	680.72 min	6
CT8	MD-Raw	55.62 min	683.65 min	6
ST2	MD-Comp02	10.52 min	680.12 min	12
ST8	MD-Comp02	42.85 min	680.72 min	7
CT8	MD-Comp02	50.18 min	683.65 min	11
ST2	MD-Comp01	10.22 min	679.45 min	14
ST8	MD-Comp01	43.01 min	680.72 min	10
CT8	MD-Comp01	50.34 min	683.65 min	17
ST2	MD-Proc	7.04 min	679.03 min	3433
ST8	MD-Proc	28.93 min	679.00 min	3694
CT8	MD-Proc	31.82 min	679.08 min	3346

5 Discussion

In the discussion section, we address several critical considerations and potential extensions of our study:

Approximated Area of Interest. Firstly, the area of interest (AOI) analyzed—Argentina's maritime region—was approximated. While the exact boundary details may evolve, our models predict that the broader conclusions about data handling and satellite operations will hold within the specified fishing area. However, a more tailored adaptation of the model would be required to extend our analysis to other regions with similar challenges, such as Peru and Ecuador, where illegal fishing is also of concern.

Fleet Size. Our current study focused on a small constellation of three satellites. Expanding this constellation would necessitate a comprehensive update to the framework and operational models, particularly those centered around a master satellite configuration. While increasing the number of satellites could enhance coverage and data acquisition capabilities, it would also introduce additional complexity to the swarm's coordination and data relay strategies. Furthermore, there is room to evaluate configurations like AT120, where satellites are distributed across vast regions, even considering entire swarms distanced every 120 degrees in angular separation.

Research in Automated Operations. Regarding future research directions, our operation modes, while functional, are recognized as relatively simplistic. The investigation highlighted promising avenues for research in automated, energy-aware Inter-Satellite Link (ISL) and payload duty cycling. Such features are especially relevant for a 100 kg-class spacecraft equipped with a Synthetic Aperture Radar (SAR) payload, where efficient resource management is vital. In this context, Delay-Tolerant Networking (DTN) architectures and the derived Bundle Protocol (BP) can play a decisive role.

Research in Onboard Processing. Additionally, the preliminary quantification of on-board classification underscores the potential for further investigation into on-board data processing. This includes the challenges of implementing machine learning inference directly on the satellite and the associated issues of model training and dataset procurement from the ground—a frontier area in satellite data handling that beckons exploration.

Evaluation Framework. We provide a versatile toolchain to accommodate different assumptions and enable the exploration of various trade-offs. This facilitates the replication or extension of our analysis under different conditions—whether they involve other regions' AOIs, varying satellite orbital parameters, or alternative satellite constellations—offering a broad utility for future mission planning and research within the Segmented Architecture program and beyond.

Mission-Specific Evaluation. It is important to note that this paper presents a static analysis of system performance based on general coverage metrics. While this approach helps establish baseline capabilities, a more detailed mission-driven analysis, such as an Observing System Simulation Experiment (OSSE) [69], would be necessary to evaluate the system's performance in realistic mission scenarios. Due to space constraints, incorporating such an approach is left as future work, where we plan to simulate dynamic mission conditions, such as vessel tracking in maritime surveillance, to assess the system's operational effectiveness further.

6 Conclusions

The landscape of satellite architectures is witnessing a transformative shift towards segmented, cooperative configurations, exemplified by CONAE's pioneering Segmented Architecture (SA) program. This study has provided a quantitative analysis of such architectures in the context of the MISSION project, leveraging a suite of dynamic models within the Systems Toolkit (STK) environment. Our investigation's insights reveal the intricate trade-off between satellite formations, the complexities of contact dynamics, and the calculus of data handling strategies, all of which inform the operational framework of our proposed SARE mission.

Our findings underscore the equilibrium between swarm configuration and coverage efficiency. The innovative segmented architecture allows for strategic flexibility yet requires careful planning to maximize the observational potential. While more minor angular separations present dense swarms that assure frequent but clustered access, larger separations offer more evenly spaced coverage, albeit with more significant intervals. The selection of swarm configuration emerges as a critical decision point that hinges on mission-specific requirements. It balances the quest for persistent surveillance with the constraints of technological capabilities, primarily limited by Inter-Satellite Links (ISLs) capacity.

The contact analysis within our study elucidates the promising prospects of extended coverage over Argentina's EEZ while also surfacing the challenges posed by data offloading, particularly under constrained operational conditions. The varying performances of the ST2, ST8, and CT8 configurations in managing ISL ranges and data rates highlight the importance of a tailored approach to

constellation design. This affirms that the SA program's architecture must be as dynamic and adaptable as the maritime activities it endeavors to monitor.

Looking forward, the field of automated, energy-aware ISL management and on-board classification strategies beckons further research. A particularly promising avenue is the potential for onboard processing to mitigate the limitations of data transfer capacity, especially in light of the 100 kg-class spacecraft constraints. These strategies exemplify the SA program's innovative spirit and serve as a beacon for future missions aiming to harness the full potential of segmented satellite architectures.

Our study, although expansive, stands on the threshold of an even more extensive realm of exploration. As we chart the course for subsequent endeavors, we leave a trail of comprehensive models and analysis tools, inviting others to extend and enrich the fabric of segmented satellite architecture research. The SA program's journey is far from over.

Acknowledgments

This project has received funding from the European Union's Horizon 2020 research and innovation program under the Marie Skłodowska-Curie grant agreement No 101008233 (MISSION) and the French National Research Agency (ANR) under the project ANR-22-CE25-0014-01.

References

[1] CONAE. 2023. Arquitectura segmentada: un nuevo paradigma espacial. Retrieved Mar. 2, 2024 from https://www.argentina.gob.ar/noticias/arquitectura-segmentada-un-nuevo-paradigma-espacial.

[2] Andrés López, Paulo Pascuini, and Adrián Ramos. 2019. Economía del espacio y desarrollo: el caso argentino. *Revista Iberoamericana de Ciencia, Tecnología y Sociedad-CTS*, 14, 40, 111–133. https://hdl.handle.net/11336/119725.

[3] Oltjon Kodheli et al. 2021. Satellite communications in the new space era: A survey and future challenges. *IEEE Communications Surveys & Tutorials*, 23, 1, 70–109. DOI: 10.1109/COMST.2020.3028247.

[4] Alberto E. Giraldez. 2004. SAOCOM-1 Argentina L-band SAR mission overview. In *Proceedings of the 2nd Workshop on Coastal and Marine Applications of SAR (CMASAR)* (ESA Special Publication). Vol. 565.

[5] Amit Sen, Yunjin Kim, Daniel Caruso, Gary Lagerloef, Raul Colomb, Simon Yueh, and David Le Vine. 2006. Aquarius/SAC-D mission overview. In *Sensors, Systems, and Next-Generation Satellites X*. Vol. 6361. SPIE, 63610I. DOI: 10.1117/12.691981.

[6] Juan A. Fraire, Pablo G. Madoery, Jorge M. Finochietto, Pablo A. Ferreyra, and Raoul Velazco. 2016. Internetworking approaches towards along-track segmented satellite architectures. In *2016 IEEE International Conference on Wireless for Space and Extreme Environments (WiSEE)*. IEEE, 123–128. DOI: 10.1109/WISEE.2016.7877316.

[7] Milko Schvartzman. 2022. Disclosed: changes in china's high seas fishing patterns | south pacific vs. south atlantic geopolitics. Retrieved Mar. 2, 2024 from https://seafood.media/fis/worldnews/worldnews.asp?id=120821.

[8] Tianwen Zhang et al. 2021. SAR ship detection dataset (SSDD): official release and comprehensive data analysis. *Remote Sensing*, 13, 18, 3690. DOI: 10.3390/RS13183690.

[9] Urška Kanjir, Harm Greidanus, and Krištof Oštir. 2018. Vessel detection and classification from spaceborne optical images: a literature survey. *Remote Sensing of Environment*, 207, 1–26. DOI: 10.1016/j.rse.2017.12.033.

[10] David J. Crisp. 2004. The state-of-the-art in ship detection in synthetic aperture radar imagery. Research report DSTO-RR-0272. DSTO Information Sciences Laboratory, Edinburgh, Australia.

[11] Meisam Amani et al. 2022. Ocean remote sensing techniques and applications: a review (part i). *Water*, 14, 21, 3400. DOI: 10.3390/w14213400.

[12] Oscar Sommervold, Michele Gazzea, and Reza Arghandeh. 2023. A survey on SAR and optical satellite image registration. *Remote Sensing*, 15, 3, 850. DOI: 10.3390/rs15030850.

[13] 2024. Ansys Systems Tool Kit (STK). Retrieved July 1, 2024 from https://www.ansys.com/products/missions/ansys-stk.

[14] Nicholas H. Cramer, Daniel Cellucci, Caleb Adams, Adam Sweet, Mohammad Hejase, Jeremy D. Frank, Richard Levinson, Sergei Gridnev, and Lara Brown. 2021. Design and testing of autonomous distributed space systems. In *Proceedings of the AIAA/USU Conference on Small Satellites*. https://digitalcommons.usu.edu/smallsat/2021/all2021/129/.

[15] Boris Andrievsky, Alexander M. Popov, Ilya Kostin, and Julia Fadeeva. 2022. Modeling and control of satellite formations: a survey. *Automation*, 3, 3, 511–544. DOI: 10.3390/automation3030026.

[16] D.P. Scharf, F.Y. Hadaegh, and S.R. Ploen. 2003. A survey of spacecraft formation flying guidance and control (part 1): guidance. In *Proceedings of the 2003 American Control Conference*. Vol. 2, 1733–1739. DOI: 10.1109/ACC.2003.1239845.

[17] Kyle T. Alfriend, Srinivas R. Vadali, Pini Gurfil, Jonathan P. How, and Louis S. Breger. 2010. *Spacecraft Formation Flying: Dynamics, control and navigation*. Butterworth-Heinemann, Oxford. ISBN: 978-0-7506-8533-7. DOI: 10.1016/C2009-0-17485-8.

[18] James R. Wertz. 2001. *Mission Geometry; Orbit and Constellation Design and Management*. Springer Dordrecht. Chap. 13, 671. ISBN: 978-0-7923-7148-9.

[19] Harry W. Jones. 2018. The recent large reduction in space launch cost. In *48th International Conference on Environmental Systems*. https://hdl.handle.net/2346/74082.

[20] Zaher M. Kassas, Sharbel Kozhaya, Haitham Kanj, Joe Saroufim, Samer W. Hayek, Mohammad Neinavaie, Nadim Khairallah, and Joe Khalife. 2023. Navigation with multi-constellation LEO satellite signals of opportunity: Starlink, OneWeb, Orbcomm, and Iridium. In *2023 IEEE/ION Position, Location and Navigation Symposium (PLANS)*, 338–343. DOI: 10.1109/PLANS53410.2023.10140066.

[21] Christopher John Lowe and Malcolm Macdonald. 2020. Space mission resilience with inter-satellite networking. *Reliability Engineering & System Safety*, 193, 106608. DOI: 10.1016/J.RESS.2019.106608.

[22] Phillip Keane. 2018. SpaceX Starlink constellation. Retrieved Mar. 17, 2024 from https://www.engineering.com/spacex-starlink-constellation/.

[23] P. Rochelle. 2016. ORBCOMM announces commercial service for its final 11 OG2 satellites. Retrieved July 1, 2024 from https://spacenews.com/orbcomm-announces-commercial-service-for-its-final-11-og2-satellites/.

[24] M. Sheetz. 2018. Finnish startup ICEYE is building the world's largest constellation of tiny satellites to see through clouds. Retrieved July 1, 2024 from https://www.cnbc.com/2018/06/01/iceye-building-worlds-largest-sar-constellation-with-microsatellites.html.

[25] Tom Hogue. 2020. China puts final satellite for beidou network into orbit. Retrieved Mar. 17, 2024 from https://financialpost.com/pmn/business-pmn/china-puts-final-satellite-for-beidou-network-into-orbit-state-media.

[26] Rebecca Pool. 2021. Scrapheap in the sky: rising levels of space debris threaten to obliterate satellites and knockout internet access. meet the organisations racing to stop the junk in its tracks. *Engineering & Technology*, 16, 3, 44–47. DOI: 10.1049/et.2021.0309.

[27] James Osborn, Laurence Blacketer, Matthew J. Townson, and Ollie J. D. Farley. 2022. Astrosat: forecasting satellite transits for optical astronomical observations. *Monthly Notices of the Royal Astronomical Society*, 509, 2, 1848–1853. DOI: 10.1093/mnras/stab3003.

[28] Daniel M. Murphy, Maya Abou-Ghanem, Daniel J. Cziczo, and Xiaoli Shen. 2023. Metals from spacecraft reentry in stratospheric aerosol particles. *Proceedings of the National Academy of Sciences*, 120, 43. Mark Thiemens, (Ed.) DOI: 10.1073/pnas.2313374120.

[29] European Space Agency. 2014. Sentinel-1 satellite constellation. Retrieved Mar. 17, 2024 from https://www.esa.int/Applications/Observing_the_Earth/Copernicus/Sentinel-1/Satellite_constellation.

[30] P. Gamba, M.L. Carranza, G. Laneve, M. Scavuzzo, and A. Ferral. 2023. The ITAREO project: sentinel and SIASGE constellations for sdg mapping. In *IEEE International Geoscience and Remote Sensing Symposium*, 903–906. DOI: 10.1109/IGARSS52108.2023.10281922.

[31] Gabriel Maiolini Capez, Santiago Henn, Juan A. Fraire, and Roberto Garello. 2022. Sparse satellite constellation design for global and regional direct-to-satellite IoT services. *IEEE Transactions on Aerospace and Electronic Systems*, 58, 5, 3786–3801. DOI: 10.1109/TAES.2022.3185970.

[32] Veronica L. Foreman, Jacqueline Le Moigne, and Olivier De Weck. 2016. A survey of cost estimating methodologies for distributed spacecraft missions. In *AIAA SPACE 2016*. DOI: 10.2514/6.2016-5245.

[33] L. S. Breger, G. Inalhan, M. Tillerson, and J. P. How. 2006. Cooperative spacecraft formation flying: model predictive control with open- and closed-loop robustness. In *Modern Astrodynamics*. Elsevier Astrodynamics Series. Vol. 1, 237–277. DOI: 10.1016/S1874-9305(07)80010-0.

[34] Cristian Rossi, Fernando Rodriguez Gonzalez, Thomas Fritz, Nestor Yague-Martinez, and Michael Eineder. 2012. TanDEM-X calibrated raw DEM generation. *ISPRS Journal of Photogrammetry and Remote Sensing*, 73, 12–20. DOI: 10.1016/j.isprsjprs.2012.05.014.

[35] J. Gangestad, B. Hardy, and D. Hinkley. 2013. Operations, orbit determination, and formation control of the aerocube-4 cubesats. In *Proceedings of the AIAA/USU Conference on Small Satellites*. https://digitalcommons.usu.edu/smallsat/2013/all2013/116/.

[36] G. Bonin, N. Roth, S. Armitage, B. Risi, and R. Zee. 2013. The CanX-4&5 formation flying mission: a technology pathfinder for nanosatellite constellations. In

Proceedings of the AIAA/USU Conference on Small Satellites. https://digitalcommons.usu.edu/smallsat/2013/all2013/19/.

[37] European Space Agency. 2014. AeroCube 7-OCSD-A (AeroCube 7 – Optical Communication and Sensor Demonstration-A). Retrieved Mar. 17, 2024 from https://www.eoportal.org/satellite-missions/aerocube-ocsd.

[38] European Space Agency. 2014. Proba 3 mission. Retrieved Mar. 17, 2024 from https://www.esa.int/Enabling_Support/Space_Engineering_Technology/Proba_Missions/Proba-3_Mission3.

[39] Jihe Wang and Shinichi Nakasuka. 2012. Cluster flight orbit design method for fractionated spacecraft. *Aircraft Engineering and Aerospace Technology*, 84, 330–343. DOI: 10.1108/00022661211255511.

[40] Linghong Chi, Fei Sun, Zhenhua Liu, and Chuanwen Lin. 2020. Overview of fractionated spacecraft technology. In *International Conference on Computer Engineering and Application (ICCEA)*, 689–692. DOI: 10.1109/ICCEA50009.2020.00150.

[41] Jacqueline Le Moigne, John Carl Adams, and Sreeja Nag. 2020. A new taxonomy for distributed spacecraft missions. *IEEE Journal of Selected Topics in Applied Earth Observations and Remote Sensing*, 13, 872–883. DOI: 10.1109/JSTARS.2020.2964248.

[42] Kaitlin Dennison, Nathan Stacey, and Simone D'Amico. 2023. Autonomous asteroid characterization through nanosatellite swarming. *IEEE Transactions on Aerospace and Electronic Systems*, 59, 4, 4604–4624. DOI: 10.1109/TAES.2023.3245997.

[43] Hemani Kaushal and Georges Kaddoum. 2017. Optical communication in space: challenges and mitigation techniques. *IEEE Communications Surveys & Tutorials*, 19, 1, 57–96. DOI: 10.1109/COMST.2016.2603518.

[44] Toni Tolker-Nielsen and Gotthard Oppenhaeuser. 2002. In-orbit test result of an operational optical intersatellite link between ARTEMIS and SPOT4, SILEX. In *Free-Space Laser Communication Technologies XIV*. Vol. 4635. SPIE. DOI: 10.1117/12.464105.

[45] Mehtab Singh, Ina Singh, and Amit Grover. 2022. Performance analysis of a manchester encoded inter-satellite optical wireless communication link. In *2022 IEEE Conference on Interdisciplinary Approaches in Technology and Management for Social Innovation (IATMSI)*. DOI: 10.1109/IATMSI56455.2022.10119287.

[46] Ryuichi Hirayama and Shinichi Nakasuka. 2022. Analysis of tracking gimbal angles for inter-satellite optical communication system between two orbits. In *2022 IEEE International Conference on Space Optical Systems and Applications (ICSOS)*, 107–112. DOI: 10.1109/ICSOS53063.2022.9749738.

[47] Haitao Li, Xiangwen Chen, Haifeng Zhang, and Xinfang Cui. 2022. High-precision speed control for low-speed gimbal systems using discrete sliding mode observer and controller. *IEEE Journal of Emerging and Selected Topics in Power Electronics*, 10, 3, 2871–2880. DOI: 10.1109/JESTPE.2021.3125454.

[48] Faisal Fogle, Ondrej Cierny, Paula do Vale Pereira, William Kammerer, and Kerri Cahoy. 2020. Miniature optical steerable antenna for intersatellite communications liquid lens characterization. In *2020 IEEE Aerospace Conference*. DOI: 10.1109/AERO47225.2020.9172448.

[49] Otilia Popescu. 2017. Power budgets for cubesat radios to support ground communications and inter-satellite links. *IEEE Access*, 5, 12618–12625. DOI: 10.1109/ACCESS.2017.2721948.

[50] Heather Welch, Tyler Clavelle, Timothy D. White, Megan A. Cimino, Jennifer Van Osdel, Timothy Hochberg, David Kroodsma, and Elliott L. Hazen. 2022. Hot spots of unseen fishing vessels. *Science Advances*, 8, 44, eabq2109. DOI: 10.1126/sciadv.abq2109.

[51] MarineTraffic. 2024. Screenshot of MarineTraffic website. Retrieved Mar. 17, 2024 from https://www.marinetraffic.com.

[52] VENG. 2024. Ground segment services. Veng. Retrieved Mar. 27, 2024 from https://www.veng.com.ar/en/servicio_segmentoterreno.

[53] Sung Wook Paek, Sangtae Kim, Luzius Kronig, and Olivier de Weck. 2020. Sun-synchronous repeat ground tracks and other useful orbits for future space missions. *The Aeronautical Journal*, 124, 1276, 917–939. DOI: 10.1017/aer.2020.21.

[54] Arsenios Tsokas, Maciej Rysz, Panos M. Pardalos, and Kathleen Dipple. 2022. SAR data applications in earth observation: an overview. *Expert Systems with Applications*, 205, 117342. DOI: 10.1016/j.eswa.2022.117342.

[55] Domenico Velotto, Matteo Soccorsi, and Susanne Lehner. 2014. Azimuth ambiguities removal for ship detection using full polarimetric X-band SAR data. *IEEE Transactions on Geoscience and Remote Sensing*, 52, 1, 76–88. DOI: 10.1109/TGRS.2012.2236337.

[56] Roberto Del Prete, Maria Daniela Graziano, and Alfredo Renga. 2023. Unified framework for ship detection in multi-frequency SAR images: a demonstration with COSMO-SkyMed, Sentinel-1, and SAOCOM data. *Remote Sensing*, 15, 6, 1582. DOI: 10.3390/rs15061582.

[57] Gellert Mattyus. 2013. Near real-time automatic marine vessel detection on optical satellite images. *The International Archives of the Photogrammetry, Remote Sensing and Spatial Information Sciences*, XL-1/W1, 233–237. DOI: 10.5194/isprsarchives-XL-1-W1-233-2013.

[58] Tamer Saleh, Shimaa Holail, Xingxing Weng, Xiongwu Xiao, and G-S Xia. 2023. Ship detection in COSMO-SkyMed SAR imagery using a novel CNN-based detector: a case study from the suez canal. *ISPRS Annals of the Photogrammetry, Remote Sensing and Spatial Information Sciences*, X-1/W1-2023, 715–722. DOI: 10.5194/isprs-annals-X-1-W1-2023-715-2023.

[59] Joao A. Lorenzzetti, Rafael L. Paes, and Douglas M. Gheradi. 2010. A performance comparison of a CFAR ship detection algorithm using EnviSat, RadarSat, COSMO-SkyMed and Terra SAR-X images. In *Proceedings of SeaSAR 2010 Workshop* (ESA Special Publication). Vol. 679.

[60] Armando Marino and Pasquale Iervolino. 2017. Ship detection with COSMO-SkyMed PINGPONG data using the dual-pol ratio anomaly detector. In *2017 IEEE International Geoscience and Remote Sensing Symposium (IGARSS)*. IEEE, 3897–3900. DOI: 10.1109/IGARSS.2017.8127853.

[61] Natalia V. Revollo and Claudio A. Delrieux. 2017. Vessel and oil spill early detection using COSMO satellite imagery. In *Remote Sensing of the Ocean, Sea Ice, Coastal Waters, and Large Water Regions 2017*. Vol. 10422. SPIE. DOI: 10.1117/12.2279545.

[62] Claudio Augusto Delrieux, Pablo Odorico, Lucas Rodríguez, Marina Paola Cipolletti, and Diego Marcovecchio. 2016. Real-time vessel and oil spill detection in the argentine ocean littoral using SAR satellite imagery. *Indian Journal of Geo-Marine Sciences (IJMS)*, 45, 9, 1101–1109. https://nopr.niscpr.res.in/handle/123456789/35207.

[63] Gregory Stock, Juan A. Fraire, H. Hermanns, E. Cruz, I. Alastair, and Z. Imbrosh. 2021. On the automation, optimization and in-orbit validation of intelligent satellite constellation operations. In *Proceedings of the AIAA/USU Conference on Small Satellites*. https://digitalcommons.usu.edu/smallsat/2021/all2021/168/.

[64] Gregory Stock, Juan A. Fraire, Tobias Mömke, Holger Hermanns, Fakhri Babayev, and Eduardo Cruz. 2020. Managing fleets of LEO satellites: nonlinear, optimal, efficient, scalable, usable, and robust. *IEEE Transactions on Computer-Aided Design of Integrated Circuits and Systems*, 39, 11, 3762–3773. DOI: 10.1109/TCAD.2020.3012751.

[65] J. A. Fraire, G. Nies, H. Hermanns, K. Bay, and M. Bisgaard. 2018. Battery-aware contact plan design for LEO satellite constellations: the Ulloriaq case study. In *2018 IEEE Global Communications Conference (GLOBECOM)*. DOI: 10.1109/GLOCOM.2018.8647822.

[66] James V. Stone. 2015. *Information Theory: A Tutorial Introduction*. Sebtel Press. ISBN: 978-0-9563728-5-7.

[67] Athanasios Vasilakos, Yan Zhang, and Thrasyvoulos Spyropoulos. 2016. *Delay tolerant networks*. CRC Press. ISBN: 978-1-4398-1112-2.

[68] Marius Feldmann, Juan A. Fraire, Felix Walter, and Scott C. Burleigh. 2022. Ring road networks: access for anyone. *IEEE Communications Magazine*, 60, 4, 38–44. DOI: 10.1109/MCOM.001.2100835.

[69] Charles P. Arnold Jr. and Clifford H. Dey. 1986. Observing-systems simulation experiments: past, present, and future. *Bulletin of the American Meteorological Society*, 67, 6, 687–695. DOI: 10.1175/1520-0477(1986)067<0687:OSSEPP>2.0.CO;2.